NTNU
Institutt for materialteknologi

Bachelor thesis

Monitoring of Emulsion Stability in a Stirred Tank Cell System

---

Analyse av emulsjonsstabilitet i røretank

Project number: IMA-B-2-2022

Authors:
Marcus Oppebøen Vaadal & Snorre Kværnø Sæther

Internal advisor: **Gerhard H. Olsen**

External advisor: **Amit Patil**

Employer: **SINTEF**

Grade: **Open**

20. May, 2022

Preface

This thesis was written as a final work of a bachelor's degree in chemical engineering at the Department of Material Science and Engineering at the Norwegian University of Science and Technology, NTNU. The work was done with the help and resources of the research-project IMPOSE at SINTEF Industry from January to May 2022.

We would like to express our gratitude to;

Amit Patil, at SINTEF Industry, for guidance in literature, theory and experimental work.

Bendik Sægrov-Sorte, at SINTEF Industry, for the engineering and help regarding the stirred tank cell system.

Gerhard H. Olsen, at NTNU, for the help in writing this work and for all the short and the long meetings.

Trondheim, May 20. 2022

X Snorre Sæther

Snorre Kværnø Sæther

X Marcus Oppebøen Vaadal

Marcus Oppebøen Vaadal

Abstract

The goal of this work is testing a stirred tank cell system, containing a video microscope used in measuring droplet size distribution, and further developing a float system for measuring height evolution of a dense packed layer.

The stirred tank cell system was further developed from a previous design. This new system was capable of measuring energy input, dense packed layer height and droplet size distribution. Experiments were done with both Exxsol D80, 20 ppm and Exxsol D80 60 ppm with Span83 as the surfactant. Each at seven watercuts. A stirrer was used to create emulsions in the system, which was then monitored by a float system to determine dense packed layer evolution. A particle video microscope developed at SINTEF Industry was used to capture images of the emulsion. These images were analysed both with a SSD-lite neural network and a filtered Hough algorithm. From these results the capabilities of this stirred tank cell is displayed.

The old and new float iterations were compared against each other and it was found that the new float proved significantly more stable. A problem with the new floats were found when it could not measure height accurately at the top and bottom of the tank. Plots of droplet size distribution and dense packed layer evolution showed fairly good correspondence to the changes in impeller speed.

Sauter mean diameter of droplets at equilibrium was compared to the Kolmogorov length scale and all emulsion equilibrium were determined to be in the inertial subrange. From this inertial subrange plots were fitted and inertial coefficients and intercepts were found. The inertial coefficients for oil in water emulsions at 20 and 60 ppm indicated a more stable emulsion than that of water in oil emulsions. The inertial intercepts indicated that emulsions at 20 ppm had higher droplet rigidity than that of emulsions at 60 ppm.

Sammendrag

Målet med dette arbeidet er utprøving av et røretank system som inneholder et video mikroskop benyttet i måling dråpe størrelse distribusjon, og videreutvikling av et flotør system for måling av tettpaknings lag høyde.

I dette arbeidet ble et røretank system videreutviklet fra tidligere iterasjon. Dette nye systemet hadde mulighet til å måle tilført energi, tettpaknings lag og distribusjon av dråpestørrelse. Forsøk ble gjennomført med både Exxsol D80 (20 ppm) og Exxsol D80 (60 ppm) med Span83 som surfaktant. Begge konsentrasjoner ble testet på syv vann-olje fraksjoner. En rører ble benyttet til å lage emulsjoner i systemet, som deretter målte utviklingen av tettpaknings lag. En partikkel video mikroskop probe utviklet av SINTEF Industri ble benyttet til å hente inn bilder av emulsjonen. Disse bildene ble analysert både med SSD-lite neural nettverk og en filtrert Hough algoritme.

De gamle og nye flotørene ble sammenlignet og det ble funnet at de nye flotørene var mer stabile. Et problem med de nye flotørene ble oppdaget da de ikke kunne måle hele tankhøyden nøyaktig. Distribusjon av dråpestørrelse og tettpaknings lag utvikling viste utvikling i tråd med endringer i impeller hastighet.

Sauter mean diameter av dråper ved likevekt ble sammenlignet med Kolmogorov lengde skala og alle emulsjoner ved likevekt ble bestemt til å ligge i inertial subrange. Fra dette ble inertial subrange plottet og inertial koeffisient og skjæring ble funnet. De inertiale koeffisientene for olje i vann emulsjon ved 20 og 60 ppm indikerte en mer stabil emulsjon enn for vann i olje emulsjon. De inertiale skjæringene indikerte at emulsioner ved 20 ppm hadde høyere dråpe stivhet enn emulsjoner ved 60 ppm.

Table of Contents

List of symbols

- D_{smd} = average particle or droplet diameter in fluid system
- C_i = inertial coefficient
- σ = interfacial tension
- ρ_c = density of the continous phase
- ϵ = dissipation energy
- $D_{\text{smd}i0}$ = inertial droplet size intercept
- C_v = viscous coefficient
- v = kinematic viscosity of the continous phase
- $D_{\text{smd}v0}$ = viscous droplet size intercept
- η = viscosity
- P = power input
- V_t = tank volume
- D_a = impeller diameter
- α = ratio of impeller velocity over impeller tip velocity
- N_Q = flow number for the given impeller
- B_F = bouyancy force
- IØ = inner diameter
- OØ = outer diameter

Abbreviations

o/w = oil in water emulsion
w/o = water in oil emulsion
o/w/o = oil in water in oil emulsion
w/o/w = water in oil in water emulsion
WC = Water-cut
PVM = Particle video microscope
CCD = Charge-coupled device
CMOS = Complementary metal-oxide-semiconductor
CNN = Convolutions neural network
R-CNN = Regional-CNN
SSD = Single Shot Detector
DPL = Dense packed layer
FDM=fused deposit modeling
SLA=Stereolithography
SLS=Selective Laser Sintering
CNC (machining) = Computer Numerical Control
PEEK=Poly(Ether Ether Ketone)
flt_O= flotation device residing at the the oil DPL interface
flt_W= flotation device residing at the water DPL interface
MMR = Magnetostrictive measuring rod
RPM = Revolutions per minute

1 Introduction

One of the main concerns regarding emulsion formation when transporting and refining crude oil is the increase of cost and reduction of effectiveness. This is due to several problems related to emulsions of water in crude oil including, corrosion, flow blockage, and pressure drops [1, 2]. Another occurring problem is the increased water content of the oil due to emulsions. Higher water content leads to higher volumes of transport for equal amounts of oil content. It is also considered non-ideal on behalf of the refiner, due to an increased need for storage capacity following a larger total volume and increased need for refinement of the oil [2].

Ideally chemical assistance in the form of emulsion breakers should be applied as early in the process as possible. Often this happens at the wellhead but treating the emulsion down hole is ideal to give the emulsion longer contact with the treatment chemicals [2]. As the emulsion settles out what often occurs is a dense packed layer (DPL) forming. The DPL is stabilized by surfactants present in the oil and is significantly harder to separate than the rest of the emulsion. Often this fraction is then simply discarded without recovery as the methods for recovery is costly and often prove inefficient [3].

To prevent this the IMPOSE project group at SINTEF has developed and tested a emulsion stability measuring technique. The technique looks to replace the current method of using bottle tests to determine chemical treatment. Using data from this method models of emulsion systems can be created to predict their behaviour in oil pipelines. [3]

The goal of this work is testing a stirred tank cell system, containing a video microscope used in measuring droplet size distribution, and further developing a float system for measuring height evolution of a dense packed layer.

2 Theory

2.1 Emulsion theory

An emulsion can be defined as a dispersion of a liquid in another liquid, where a dispersion is described as a system of two or more immiscible phases [1]. Emulsions can be categorized into two categories depending on the composition of the emulsion. If droplets of oil is dispersed in a continuous phase of water the emulsion is called an oil in water emulsion(o/w), and likewise for water droplets dispersed in a continuous oil flow it is called a water in oil emulsion(w/o) [1].

2.1.1 Emulsion formation

The formation of emulsions follows criteria which can be summarized into three categories. The first category requires the emulsified phase and continuous phase to have adequately different solubility and molecular composition from each other [2]. It is also required by the first criterion that both phases is in their liquid state according to the definition of an emulsion [2]. Together these conditions would mean the first criterion describes the emulsion being a dispersion of two liquids. The second criterion requires the presence of intermediary agents which possess partial solubility in both phases. Intermediary agents often possess qualities of bipolarity due to functional groups, meaning they can interact with both a polar and nonpolar phase giving partial solubility in both phases [1, 2]. The third and final criterion is presence of an energy source with appropriate magnitude so as mixing of the phases can occur [1, 2].

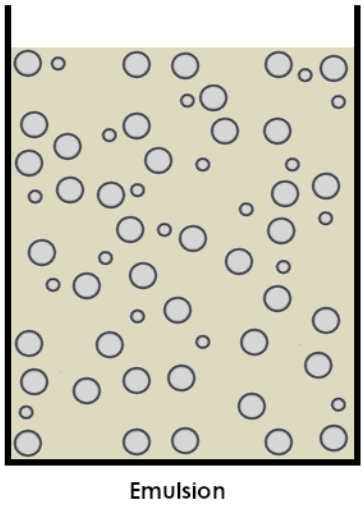

Figure 1: Illustration showing droplets of the dispersed phase in the continous phase [1].

The tendency for an emulsion to propagate as either a water in oil (w/o) or oil in water (o/w) emulsion is mainly determined by the polarity, structure of molecules, and phase ratio present in the emulsion [2]. It is also possible for an emulsion to consist of multiple emulsion otherwise known as a complex emulsion. Complex emulsions are w/o/w or o/w/o emulsions where both emulsion types are present, an example being water droplets encased by oil droplets in an aqueous phase [4]. These complex emulsions tend to form close to the inversion point of the emulsion which will be expanded on further in Section 2.1.2 [4].

2.1.2 Droplet dynamics

In general the deemulsification of an emulsion can be described by three different terms. The first term being flocculation, where droplets in the emulsion gather to form clusters functioning as a single unit. The amount and size of the droplets flocculating may vary over time for any given unit as the droplets still maintain their original shape and can leave the cluster. The second term is coalescence also known as fast flocculation. During coalescence droplets coalesce into larger droplets by collision. Droplets coalescing will eventually lead to phase separation. The third term is flocculation and coalescence together otherwise known as slow flocculation. The system described by this term has droplets flocculating (and deflocculating) into clusters which then coalesce into larger droplets. For systems of this type where the deflocculation rate is relatively high the system and emulsion will remain relatively stable. [4]

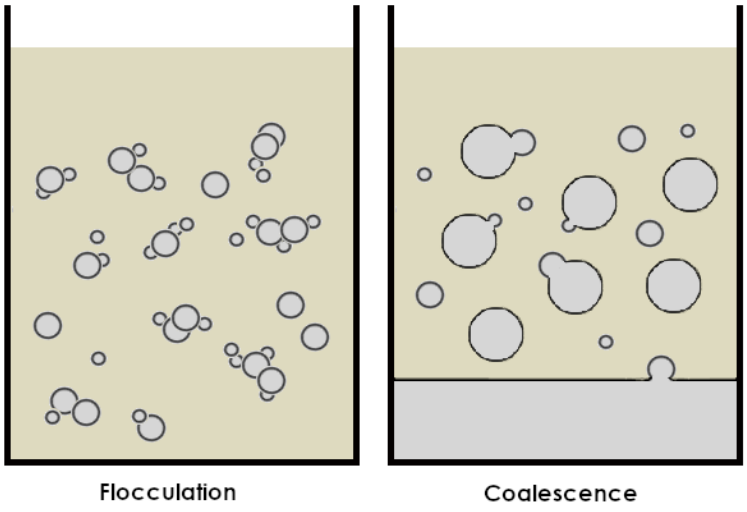

Figure 2: Illustration showing flocculation and coalescence of an emulsion [1].

Another part of droplet behaviour in emulsions is the process of settling and creaming. Simply put these processes is the movement of droplets either up or down in the solution depending on their density and the phase they reside in. If the droplet or particle rises it is considered to be creaming, and likewise for a droplet or particle sinking it is considered settling. In and of itself these processes does not

break the emulsion, but they often work with the previously mentioned methods of deemulsification to eventually break the emulsion [4].

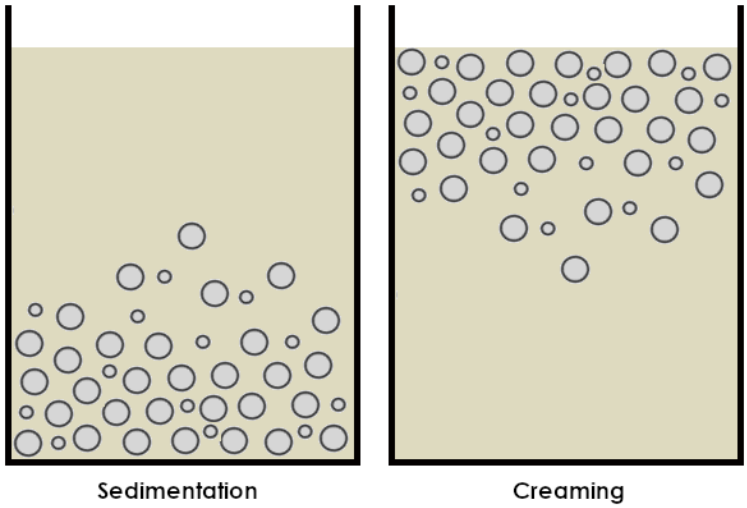

Figure 3: Illustration showing sedimentation (settling) and creaming of an emulsion [1].

Ostwald ripening can contribute to the rate of creaming and settling. Similiar to coalesence Ostwald ripening will increase the average droplet size in an emulsion, but rather than increasing droplet size by collision and coalescence it describes the effect of smaller droplets being more susceptible to partial solution in the continous phase. Since the system is in equilibirum the smaller droplets will then dissolve into the larger droplets. Over time this increases the average droplet size [4].

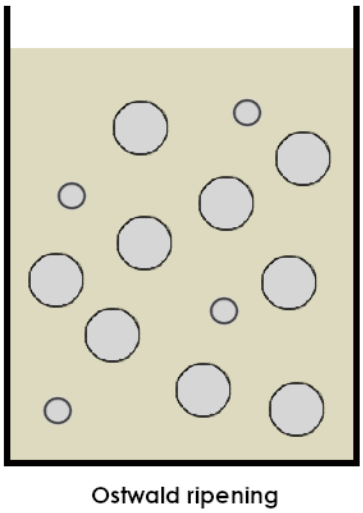

Figure 4: Illustration showing average droplet size increase due to Ostwald ripening [1].

Another process that sometimes occurs in emulsion systems is phase inversion. Simply put the emulsion inverts making the dispersed phase the continuous phase and likewise the continuous phase the dispersed phase. An example would be an o/w emulsion turning into an w/o emulsion. Phase inversion relies on the phase ratio of the emulsion. The phase ratio at which the phase will invert is called the inversion point. [4]

2.1.3 Emulsion stability

The stability of an emulsion is the ability of droplets to stay dispersed in a continuous flow [5]. Emulsion can be divided into micro- and macro- emulsions, with droplets bigger than 0.1 µm being macro-emulsions, and droplets smaller than 10 nm being micro-emulsions [1, 4]. Generally micro-emulsions are considered thermodynamically stable and occur when an emulsion is formed between two liquids with severly low interfacial tensions (less than 10^{-2} mN/m) [4]. On the other hand macro-emulsions are considered thermodynamically unstable and will over time coalesce and separate. However emulsion stabilisation can eliminate the droplet coalesence [1].

Generally droplet size distribution in emulsions is heterodisperse, meaning droplets rarely have uniform size. Droplet size and distribution can impact properties of emulsions such as, rheology, color, opacity, and stability. Measuring the rate of change of droplet distributions is therefore an important part in determining destabilization of emulsions [4].

Surface active agents (Surfactants) generally work by lowering surface tension of interfaces in solution [1]. Surfactants are amphiphillic, having a hydrophillic and a hydrophobic branch, which means they are partially soluble in both polar and nonpolar fluids . In a mixture of two immiscible phases surfactants will often adhere to the interface separating the two phases creating an interfacial film [1]. This is due to the hydrophillic end wanting to stay in the polar phase and the hydrophobic phase wanting to stay in the nonpolar phase. Another property of surfactants is their ability to stabilize emulsion by forming micelles as shown in Figure 5 [1, 5].

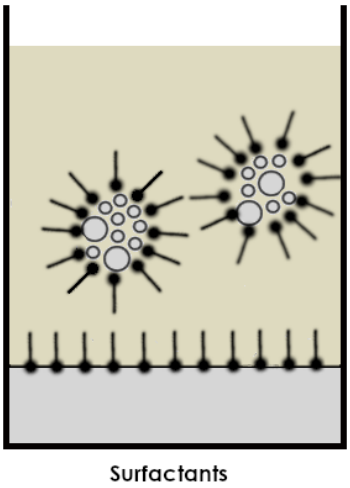

Figure 5: Illustration showing effects of surfactants forming micelles and adhering to the water-oil interface. [1]

Droplet formation leads to increased total surface area for equal volume. Due to this the effects of surface active agents will have an increased effect in emulsions [4]. Often addition of more than one type of surfactant will form a more stable emulsion based on differing stabilization properties of the surfactants [4]. In crude oil the most commmonly occuring surfactants are waxes and asphaltenes.

2.1.4 Rheology

The Reynolds number is used to identify fluid flow regimes. Flows with a Reynolds number lower than 2300 are considered laminar, and flows above 4000 are considered turbulent in pipes. Flows between laminar and turbulent are considered transitionary. Generally laminar flows are easier to work with and lends themselves to theoretical prediction, but this is not the case for transitional and turbulent flows. The equation for determining Reynolds number in a pipe is given in Equation 1: [6]

$$\mathbf{Re} = \frac{\rho v D}{\mu} \tag{1}$$

Where:

- ρ is the fluid density
- v is the fluid average velocity
- D is the pipe diameter
- μ is the fluid dynamic viscosity

As can be seen in Equation 1 the Reynolds number and therefore flow regime is dependent on the fluid viscosity. This means viscosity changes due to emulsions has the possibility to affect fluid flows.

The viscosity of an emulsion is affected by several factors including, viscosity of the continuous and dispersed phase, amount of surfactants present, droplet size distribution, temperature and shear rate [1]. The water-cut (WC) of the emulsion can also impact the viscosity. For WC over 30% w/o emulsions has been shown to exhibit significantly higher viscosity than both oil and water [1, 7].

2.1.5 Droplet relaxation

Lowering dissipation energy in the system leads to droplet relaxation, meaning increased droplet coalescence and average droplet size. After the droplets has relaxed they will reach an equilibrium droplet size [5]. Knowing this it is possible to characterize droplet relaxation behaviour based on the average droplet size measured in sauter mean diameter (D_{smd}) of the droplets [5]. D_{smd} is a measure often used in fluid dynamics to give a better estimation of the droplet sizes. This due to it favoring larger droplets over smaller droplets which often are more plentiful and thereby lowering the average. Equation 2 shows how D_{smd} is calculated.

$$D_{\text{smd}} = \frac{\sum_{i=1}^{n} D_i^3}{\sum_{i=1}^{n} D_i^2} \tag{2}$$

Where:

- D is individual droplet size

Previous work has established four different droplet relaxation profiles for oil and water emulsion systems based on the dominant force or process [5]. In systems showing fast equilibration the turbulent shear force is dominant with lower relative buoyancy force. As shown in Figure 6 the droplet size will equilibriate at a higher D_{smd}. Systems showing slow equilibration is similiar to fast equilibration but the droplet relaxation rate is slower. This is mainly due to viscosity of the fluids and/or surfactants. For systems showing unstable settling the buoyancy force is high relative to the turbulent shear forces. Here droplets will quickly reach a maximum droplet size before settling at a lower droplet size. For systems showing jamming (pickering emulsion) no further coalescence happens on dissipation relaxation as shown in Figure 6 due to surfactants. [5]

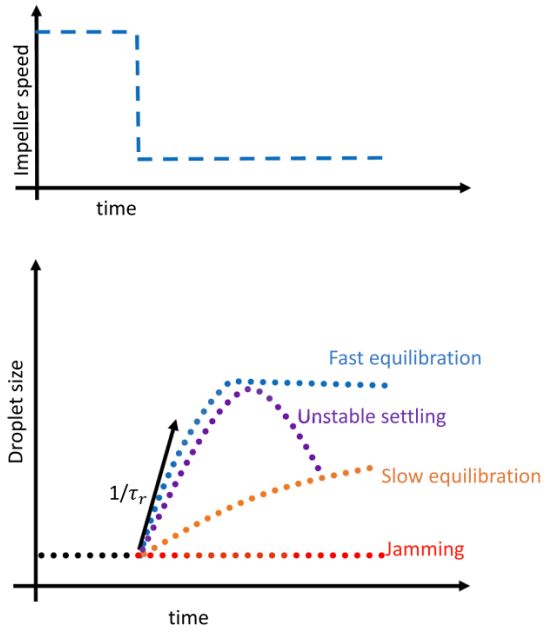

Figure 6: Droplet relaxation profiles related to impeller speed lowering found in previous work [5].

2.1.6 Inertial and viscous subrange

Considering droplet break up the inertial and viscous subrange is important. In the inertial subrange droplets are larger than the smallest eddies. Inertial forces contribute more to droplet break up in this subrange. The opposite is true for the viscous subrange where the droplets are smaller than the smallest eddies. Viscous stresses contribute more to droplet break up relative to the turbulent stresses in this subrange. This is due to high relative kinematic velocity compared to interfacial tensions. A previous work proposed two equations for characterization of emulsions given in Equation 3 for the inertial subrange and Equation 4 for the viscous subrange. [5]

$$D_{\text{smd}} = C_i(\frac{\sigma}{\rho_c})^{\frac{3}{5}}\epsilon^{\frac{-2}{5}} + D_{\text{smd}i0} \tag{3}$$

Where:

- D_{smd} is the equilibrium droplet size
- C_i is the inertial coefficient
- σ is the interfacial tension
- ρ_c is the density of the continous phase
- ϵ is the dissipation energy
- $D_{\text{smd}i0}$ is the inertial droplet size intercept

$$D_{\text{smd}} = C_v(\frac{\sigma}{\rho_c})(\epsilon v)^{\frac{-1}{2}} + D_{\text{smd}v0} \tag{4}$$

Where:

- D_{smd} is the equilibrium droplet size
- C_v is the viscous coefficient
- σ is the interfacial tension
- ρ_c is the density of the continous phase
- ϵ is the dissipation energy
- v is the kinematic viscosity of the continous phase
- $D_{\text{smd}v0}$ is the viscous droplet size intercept

Generally higher inertial or viscous coefficient would suggest the system is more stable[8]. Higher inertial or viscous intercept would suggest the droplets are more rigid [5]. To determine if an emulsion is in the inertial or viscous subrange D_{smd} at equilibrium can be plotted against the Kolmogorov length scale given by Equation 5. Droplet sizes higher than the Kolmogorov length would suggest the emulsion is in the inertial subrange, and likewise droplet sizes lower than the Kolmogorv length would suggest the emulsion is in the viscous subrange. [5]

$$l_d = (\frac{(\frac{\eta}{\rho})^3}{\epsilon})^{\frac{1}{4}} \tag{5}$$

Where:

- η is the is viscosity of the continuous phase
- ρ is the density of the continuous phase
- ϵ is the dissipation energy

The dissipation energy, ϵ can be determined by Equation 6:

$$\epsilon = \frac{P}{\rho V_t} \tag{6}$$

Where:

- P is the is power input
- ρ is the density of the continuous phase
- V_t is the tank volume

The power input, P is defined further in Section 2.2.2.

2.2 Measuring emulsion stability

To measure emulsion stability some parameters are important. One wants to observe droplet size distribution, energy input and dense packed layer (DPL) stability over time. Therefore some research groups have taken the approach of using a stirred vessel, accurately monitoring these three key parameters to increase repeatability, while also simulating real-world scenarios.

2.2.1 Stirred tank theory

Stirring vessels is an important part of both large-scale industrial production and small-scale experimental work. In experimental work vessels are usually fitted with sensors and equipment to simulate desired conditions.

When a liquid system is stirred it could either result in a miscible liquid phase forming a homogeneous solution or a dispersion when dealing with immiscible liquids.

Inside stirred vessels an impeller is situated to stir liquids. The impeller can be set up on an angle or horizontally into the vessel. The blades of the impeller can also have varying shape and angle to accommodate specialized functions of the stirring operation. Vessels can contain other inner fittings like baffles, coils, probes or feed and drainpipes.[9]

Baffles are used to interrupt flow within the vessel either to hinder vortex formation (rotation of liquid) or to create turbulent flow in the vessel. Reasons for creating a turbulent system could be to thoroughly mix liquids or to simulate real-world scenarios. Probes can observe the system inside the vessel and provide data from experiments or monitor a process. Hole perforated pipes are used to shield probes from turbulent flow, when needed. [9] In industry feed and drain pipes are common for adding reagents or nutrients and to extract product[10]. An illustration of a stirred vessel is shown in Figure 7

Figure 7: Industrial stirred tank cross-section[11]

2.2.2 Estimating energy input

Torque or rotational force is one of the basic concepts in mechanics. Torque has the SI unit N m, which is broken down to $\frac{\mathrm{kg\,m^2}}{\mathrm{s^2}}$.[12]
Torque is given by Equation 7:

$$\tau = |\mathbf{r}||\mathbf{F}| \sin\theta \tag{7}$$

where[13]:

- τ is the magnitude of torque
- r is the position vector (lever arm vector)
- F is the force vector
- θ is the angle between the force vector and the lever arm vector

This relation allow for the monitoring of energy applied to a stirred tank system by the use of a torque sensor. This is a device that is coupled to an impeller shaft and monitors the torque applied by a motor to the shaft and thereby the impeller. There are several different ways of measuring torque by sensor, the details of these are outside the scope of this work. A sensor may contain a shaft with magnetic domains. The magnetic characteristics of these magnets will change with respect to the torque[14]. The stirred tank system in this work contains this kind of sensor. Another way of measuring torque is by using a piezoelectric sensor. This sensor senses mechanical changes in a system and produces a usable electrical signal output. The signal is the product of piezoelectric crystals deformed by dynamic force. [15].

If a measure of torque and angular speed can be made the power input, P, is simply determined as shown in Equation 8:

$$P = \tau\omega \tag{8}$$

Where:

- τ is the torque applied from the impeller
- ω is the angular speed of the impeller

If no such measurement is available power can be estimated by Equation 9 [16]:

$$P = \rho n^3 D_a^5 (\frac{\alpha^2 \pi^2}{2} N_Q) \tag{9}$$

Where:

- ρ is the density of the continuous phase
- n is the impeller rotations per second
- D_a is the impeller diameter
- α is the ratio of impeller velocity over impeller tip velocity
- N_Q is the flow number for the given impeller

For stirred tank systems with baffles and regular flat blade impeller an α value of 0.95 and a N_Q value of 1.3 can be used as the values can be considered constant [16].

2.2.3 Determining droplet size distribution

A particle video microscope (PVM) can be used to determine droplet size distribution in a stirred tank. This is done through image analysis. It provides an in-situ (inside the system) direct method for determining droplet size as opposed to an in-situ indirect method. For instance there are laser systems which measure light backscattering to determine droplet size. Direct methods for analysis have an advantage over indirect methods because there is no need for translation of some physical parameter to get to the parameter one wants to measure.[17]

PVM probes can be used to measure multiple particle types. Some use cases are monitoring nucleation and dissolution behavior of crystallization in suspensions, particle measurements in emulsion polymerization and bubble size distribution in gas-liquid contactors.[17, 18]

PVM probes work by emitting near-IR lasers at an area containing particles, which is backscattered into a lense system and captures by a digital image sensor, see Figure 8. This could either be a charge-coupled device (CCD) or a complementary metal-oxide-semiconductor (CMOS) sensor, the CCD technology being outcompeted by the CMOS technology in most camera systems, while still having advantages in some areas over CMOS technology. These images can then be analysed either manually or computationally to determine droplet diameter. [17, 19]

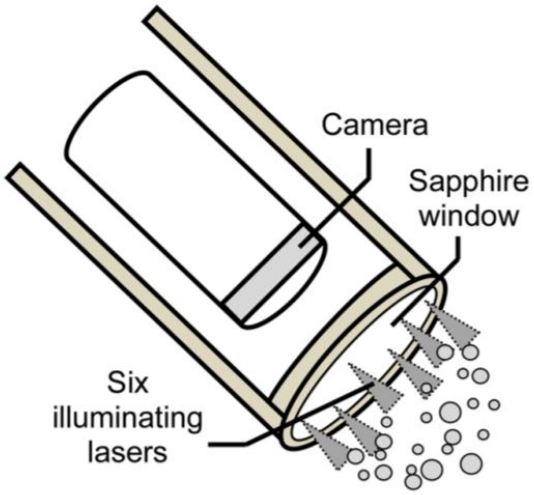

Figure 8: Illustration of PVM probe nossel[17]

One such computational method that has been used to analyse objects in images is the Hough transform. This is an algorithm that originally was designed to detect lines in images, but has been iterated upon to get a more general usage for detecting and analysing shapes in images [20]. In simple terms the Hough transform for analysing circular objects (i.e. droplets) has two stages. The first is to detect circle edges in a image and the second is to estimate center and radius of the circle [21]. A common way of detecting edges is using the "canny edge detector", which uses an edge thinning algorithm that places a criterion of gradient maxima for pixels to qualify as edges [21, 22]. The Hough transform takes points interpreted as edges and parameterize them to points in Hough space to determine parameters of a circle. It is known that the parametric Equation 10 and Equation 11 describes a circle with center at (a, b) and radius R.

$$x = a + R\cos\theta \tag{10}$$

$$y = b + R\sin\theta \tag{11}$$

The Hough Space is represented by an accumulator matrix containing such values to describe circles. This matrix contains circle candidate which is voted into the matrix from detected edges an image. In Hough space a circle border is represented by conical shapes, a point with the most overlapping cones is likely to be circles, see Figure 9. There is then found local maximas in the Hough space, representing center. Found center and edge enables the computation of radius.[20, 21]

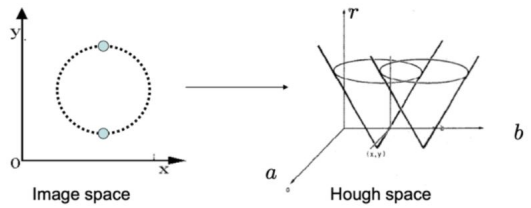

Figure 9: Transformation from image space to Hough space [23]

Detecting dispersed droplets has some inherent challenges. This includes out of focus droplets, overlapping droplets and image noise. A traditional circle Hough transform might also interpret a bubble as two circles because bubbles appear as rings in 2D-images, with an inner and an outer diameter. The properties of the liquids will also affect the analysis. For instance the opacity of the liquid will affect the light conditions of the image capture. To improve the analytical performance of the Hough transform the images are smoothed and the edges are enhanced prior to being analysed with the Hough transform.[21]

Recent work has been done to optimize the Hough transform for droplet size determination in emulsions[8]. This includes using a background image to find a suitable threshold for what data should be considered an edge and to combat false circle detection a phase angle accumulation was used. Here phase angles are voted to determine if an object contains enough phase angles to be a circle, hence a droplet.[8]

In recent times neural networks have been used to determine droplet size[8]. Neural networks are powerful tools that can be trained to influence decision-making [24]. In this context the decision which has to be made is whether an object is a circle and in what position circle center and edges are. Neural networks process data and will tweak its parameters to become more accurate over time either automatically or by manual human input. These parameters might be referred to as weights and thresholds. Neural networks are often trained by a human annotating what is relevant data for a goal output.[25]

Simply a neural network contains three layers, an input layer one or more hidden layers and a output layer, as shown in Figure 10. These layers contain nodes with associated weight and threshold. Based on these parameters a node will decide to send or not send data to the next layer of the network. The weights are added to inputs to determine the importance of any given variable. All inputs are then multiplied by their respective weights and then summed. Afterwards, the output is passed through a function which determines the output. If that output exceeds a given threshold, it activated the node, passing data to the next layer in the network. Hence the output of one node is the input of another. [24]

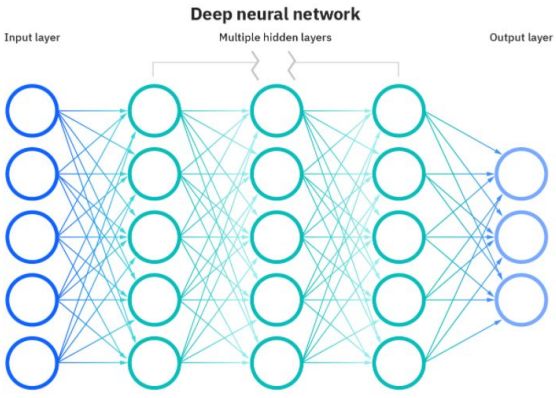

Figure 10: Illustration of connection between nodes in a neural network [24]

There are multiple neural network technologies with differing usage areas. For image classification and object recognition tasks convolutions neural networks (CNNs) are widely used. These use linear algebra, more specifically matrix multiplication, to recognize patterns in digital images. CNNs execute computationally demanding tasks, which often require graphical processing units (GPUs).[26]

To determine which CNN is more accurate and effective, they are both trained and tested on the same data sets. [8, 27]. This is a rapidly evolving field, but in 2021 one of the better CNNs was the "Faster R-CNN". This is a regional-CNN, which first extracts areas of an image containing a large complex feature, then searches this feature for containing features. A R-CNN searching for a human face in a image might first find a human and extract the area containing the human, then search the area containing the human for a human face.[27] In a recent work [8], Faster R-CNN was trained on a relevant data-set, with filtered Hough transform and manual human annotation to perform more accurately in finding droplet size than filtered Hough transform.

A light single shot detector (SSD-lite) was used in this work [28]. This particular CNN was built using the Tensor Flow lite model maker library, requiring less computational resources than a fully fledged CNN when analysing images [29, 30].

2.2.4 Measuring DPL evolution over time

In oil industry when separating petroleum products what is called dense packed layers (DPL) might be formed. This is a layer of emulsified water in oil shown in Figure 11, which is stable and slow to dissipate. The formation of a DPL is associated with coalescence of droplets and release of stabilizers from the interface of these droplets. Because of this, further coalescence is inhibited by stabilization of water droplets due to accumulation of stabilizers leading to formation of a DPL. Not much is known of the rheological properties of dense packed layers.[31]

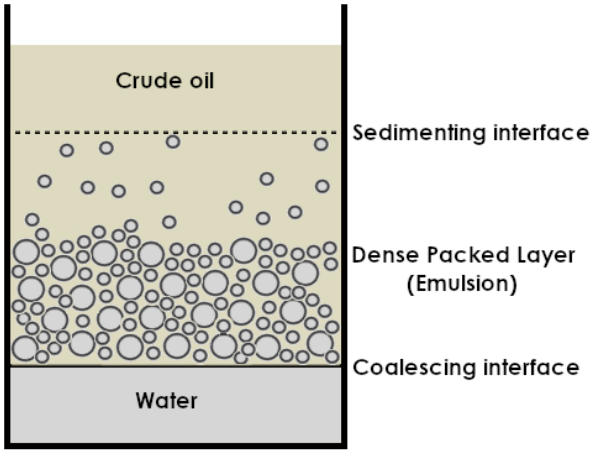

Figure 11: Drawing of DPL in water-in-crude emulsion[31]

In multiple chemical industries floats are often used to measure liquid tank level height. A float with a suited density to be buoyant on a liquid interface and some technique to measure the position of the float will tell the position of the liquid interface. [32]

Such a float is affected by Archimedes principle. When an object is submerged it experiences buoyancy force, which is the weight of the liquid displaced by the object. If the weight of this object is lower than the buoyancy force the object will float. The buoyancy force is closely related to the objects density.[13]

Density being mass in a volume simply becomes the function of buoyancy force shown in Equation 12:

$$B_F = \rho V g \tag{12}$$

Magnetostrictive measuring rods (MMRs) can be used to measure the position floats. The float fitted onto the rod carries magnets. The float position is determined by a transmitter sending a electrical signal down a sensor wire, which is often incased in some inert metal like aluminium. As the electrical signal is fired a timer circuit is activated. The electrical signal will interact with the magnetic field associated with the float. The effect of the magnetic field on the sensor wire is a generated torsional force. This force travels back to some sensor which detects the force signal (e.g. a piezoceramic sensor). The speed at which the force travels is known, when arriving back at the sensor the timing circuit is stopped and the position of the float is determined by automatic extrapolation from time and speed.[32, 33]

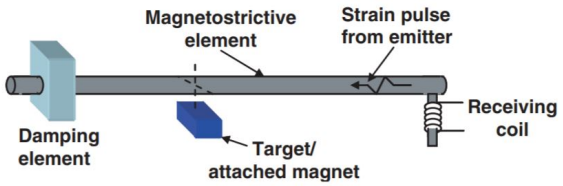

Figure 12: Illustration of magnetostricive sensor[33]

In recent times the process of engineering devices and objects which require both low time -and economic investment (e.g. prototyping) has been made more efficient by the help of 3D printing. This is a additive manufacturing technique in which a material is added layer by layer to build a wanted object. In fused deposit modeling (FDM) feed material, often some plastic, is fed into an extruder and partially melted so to be added onto the structure being manufactured. Other 3D printing techniques such as stereolithography (SLA) and selective laser sintering (SLS) are more accurate than FDM. [34, 35]

Compared to more traditional manufacturing techniques like milling or CNC machining 3D printing often allows for a quicker design process and is more efficient in use of material. Although 3D printing can be precise, resulting objects might be hard to reproduce with high accuracy, this depends on the 3D printing model[36]. High resolution 3D printing is quickly becoming more common as the field is evolving[37]. For extreme accuracy and smoother surfaces milling and CNC machining, both techniques carving objects out of solid material, might still be a better choice[36].

A common chemically resistant material used in 3D printing is nylon. Nylon is in the group of plastics called polyamides, know for being inert materials. One advantage in 3D printing nylon is its thermoplastic properties, as it will return to a hardened state keeping its properties after being melted. It is both a durable and flexible material, suitable for small structures like thin walls. A disadvantage to nylon is the hygroscopic properties, as nylon absorbs moisture.[38]

Commercial producers develop composites to be used in 3D printing. The producer MarkForge has developed the product line Onyx, which is a carbon-composite nylon. This material is reinforced with micro carbon fibres making it strong and stiff. MarkForge writes that is has a good surface finish, chemical resistivity, and heat tolerance.[39]

A plastic material used in chemical industry for its resistant to chemical degradation is Poly(Ether Ether Ketone) (PEEK). PEEK is a highly chemically resistant, heat resistant and strong material, said to be able to replace metal in some cases. [40]

3 Experimental work

3.1 Float device

3.1.1 Development of float device

From the estimated density of the DPL for Exxsol D80 and saltwater it was determined that a float (flt_O) which would settle at the oil-DPL interface should have a density of 827 $\text{kg}\,\text{m}^{-3}$. The float (flt_W) to settle at the DPL-water interface was determined in the same way and should have a density of 941 $\text{kg}\,\text{m}^{-3}$. See calculation Section A.2.

When designing all floats, sketches and 3D models were made in SolidWorks 2021. The devices were initially designed to have a torus like form, with an inner diameter(IØ) of 11 mm, outer diameter(OØ) of 20 mm and a height(h) of 10 mm. On two sides of the device holes (diameter: 3 mm, depth: 2 mm) for fitting neodymium magnets were added. Figure 13 shows 3D model (a) and 3D-printed (b) initial float (v1).

A Markforged Onyx Pro 3D-printer was used to manufacture the v1 floats. The material used was ONYX. Four devices of the above mentioned dimensions were 3D-printed and neodymium magnets were glued in place. See Table 4 for mass and density properties.

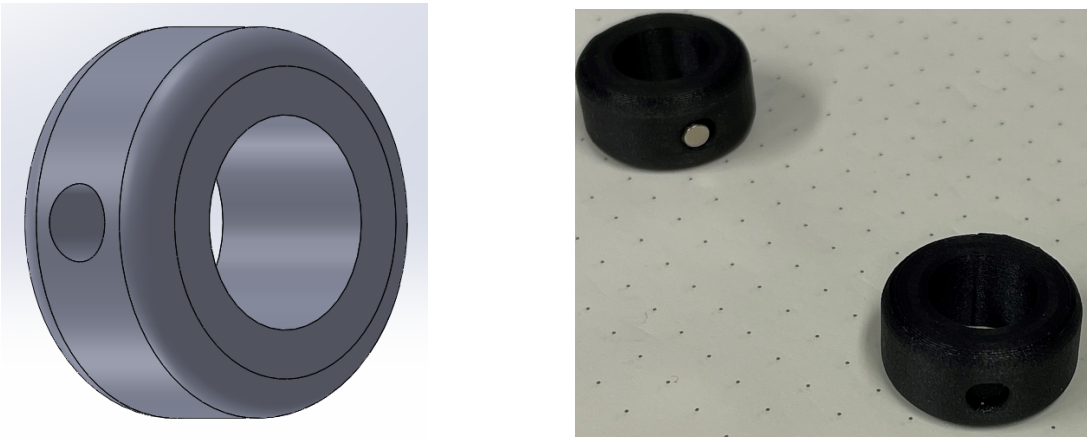

(a) (b)

Figure 13: (a) 3D model from SolidWorks 2021 and (b) 3D printed initial float design

After testing of the initial four v1 floats, six new devices were 3D-printed with considerations of experimental results. These had varying weight and with minor changes to dimensions. The dimensions of the magnet fitting holes were changed to a diameter of 4mm and a depth of 4mm. Neodymium magnets were pressure-fitted in place. Volume of the floats were found in SolidWorks, from which their density was , shown in Section B.

Further experimental results lead to a final iteration of the float device (v2). This device was machined rather than 3D-printed, and the plastic material PEEK was used. A cylindrical device with a hollow space was constructed out of three parts.

Part 1 (IØ: 11 mm, OØ: 23 mm, h: 2 mm) was made to function as a lid to be screw onto Part 2. See Figure 14 (b), number 1.

Part 2 (IØ: 11 mm, OØ: 23 mm, h: 4 mm) was constructed with four holes for adding and taking out mass and was glued onto Part 3. See Figure 14 (b), number 2.

Part 3 (IØ: 11 mm, OØ: 23 mm, h: 44 mm) was constructed as a hollow cylinder for holding the added mass. A solid section at the bottom of Part 3 was added to contain neodymium magnets. Holes were drilled through the solid section and magnets were pressure fitted in place. The remaining space behind the magnets was filled by pressure fitting material so to make the cylinder flush. See Figure 14 (b), number 3.

(a) (b)

Figure 14: (a) Top of machined float (b) side, top and bottom of machined float. Holes inside of O-rings for filling with water to add mass is seen in (a). Magnets can be seen on the bottom in (b).

3.1.2 Initial float device experiments

A temporary setup for testing the floats was put together. The setup contained two inductive measuring rods hooked to a stand, one to measure the DPL-water interface and the other to measure DPL-oil interface. An electric emulsifier(IKA T25 digital, Ultra-Turrax) was used to make the emulsions used in the setup. The rods were connected to a computer running a custom program where voltage was converted to height measurement and logged.

The initial v1 float tests simply consisted of lowering the four floats into a measuring cup filled with Exxsol D80 (450 mL) and water (100 mL) to determine which interface they would settle at. Using the electric emulsifier an emulsion was made and

the floats were lowered back in again to observe which interface they would settle at. Figure 15 illustrates this kind of experiment.

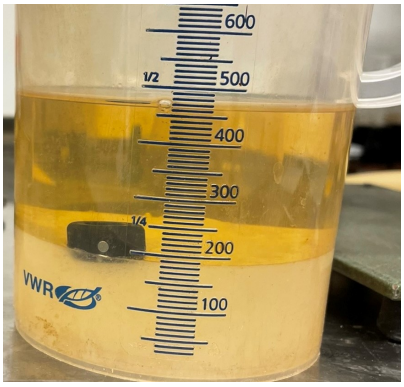

Figure 15: Float can be seen settling at the oil-water interface

Further experiments used floats from the six new 3D-printed ones. One device from the lighter three and one from the heavier three were put on their own measuring rods. An emulsion was then formed using the electric emulsifier and the data logging program was started. Several of these tests were done to find the optimal density for the floats.

3.1.3 Stirred tank cell system

For further testing of the float devices a stirred tank cell system was used. This cell system consisted of a tank (1750 mL) with five inlets and an adjustable outlet, Magnetostrictive measuring rods with floats and a video microscope custom made by the research project group IMPOSE at SINTEF. The inner diameter of the tank was 120 mm while the outer diameter of the tank lip was 180mm. The height of the tank was 157 mm. To make the tank liquid tight a gasket was made out of Viton plastic onto which a metal plate was tightened. This metal plate contained a fill hole.

Three of the inlets came out of the tank side at an 60 degree angle. Measurments of the tank can be seen in Figure 16. Two inlets were used for MMRs((Balluff MicroPulse+ BTL0UH8), (Balluff BTL12LK)), with an inner diameter of 11 mm and an outer diameter of 17 mm. The larger of the three side-inlets were made for the custom made video microscope and the two other for a PVM-probe (PVM V819). The length of the rods were 400 mm and 175 mm respectively. These sensors output a signal which was recorded on a custom computer program, saved in a ".txt" file and converted to a length unit in post. The impeller, which was connected to a stirrer(Silverson L5M-A), was a flat blade impeller with a diameter of 50 mm. There were four baffles with a width of 20 mm, 3D printed out of ONYX. The video microscope was a industry camera optimized for near IR light, which back-lights droplets at a wavelength of 810 nm. The camera was operated by a Linux computer which ran a Python program to adjust settings for lighting and image capture timing profile. Image focus was adjusted by a knob at the end of the video microscope. Image of the stirred tank cell system can be seen in Figure 17 and Figure 18

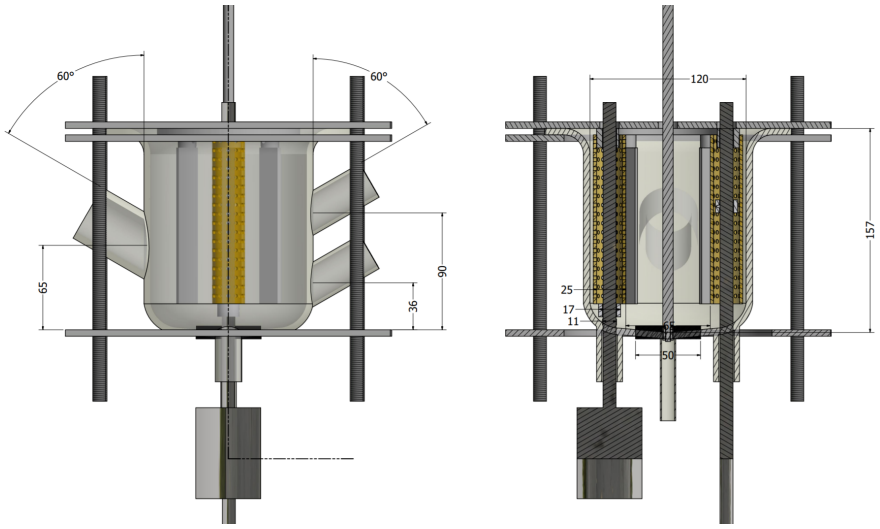

Figure 16: Cross-Section of tank with MMRs, baffles and hole perforated pipes

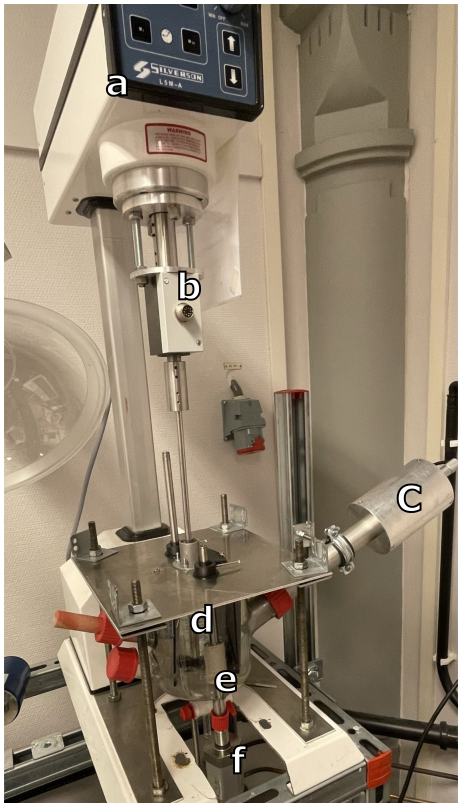

Figure 17: Stirred tank cell system; a) Stirrer, b) Torque sensor, c) Video Microscope, d) tank, e) float, f) MMR

Figure 18: Stirred Tank Cell system close-up

3.1.4 Further float device experiments

To determine performance of the v2 floats simple tests were done in the stirred tank cell system. For this and all further experiments density of $\mathrm{flt_O}$were
958 $\mathrm{kg\,m^{-3}}$ and 851 $\mathrm{kg\,m^{-3}}$ for $\mathrm{flt_W}$.

Experiments were done to compare v1 floats and v2 floats in the stirred tank cell system. 5.0 L of saline water (35 ppt salt) was made by diluting NaCl (175 g) in 5.0 L tap water in a 5 L flask. Each float design was tested at the same revolutions per minute (RPM) profile with Exxsol D80 at 99% WC, 40% WC and 1%WC. RPM profile 1 started at high RPM, then lowered to some lower RPM level, before going up to the same high RPM level, and kept on cycling like this with differing low level RPM lasting a total of 16 minutes. RPM profile 1 can be seen in Figure 19.

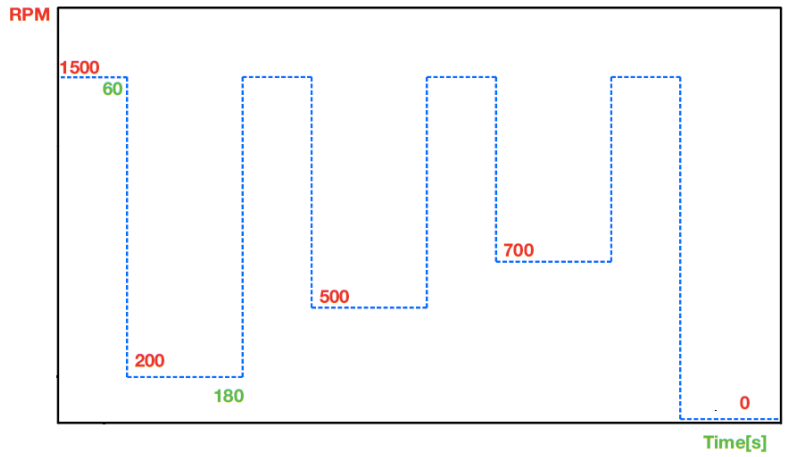

Figure 19: Graphic of RPM profile 1

MMRs with floats were used to measure DPL height, resulting data was converted to centimeter and plotted in Python.

3.2 Emulsion stability experiments

For emulsion stability experiments Exxsol D80 with surfactant Span83 was used. Emulsion was monitored by the v2 float system and video microscope, capturing 2 images in 1 second bursts every 6 seconds, resulting in a data set of 350 images when RPM profile 2 (Figure 20) was ran. Lighting and focus was adjusted by looking at the frame viewer on the Linux computer. A total of fourteen runs was done at seven different WCs and two different surfactant concentrations. The RPM profile was kept constant, seen in Figure 20

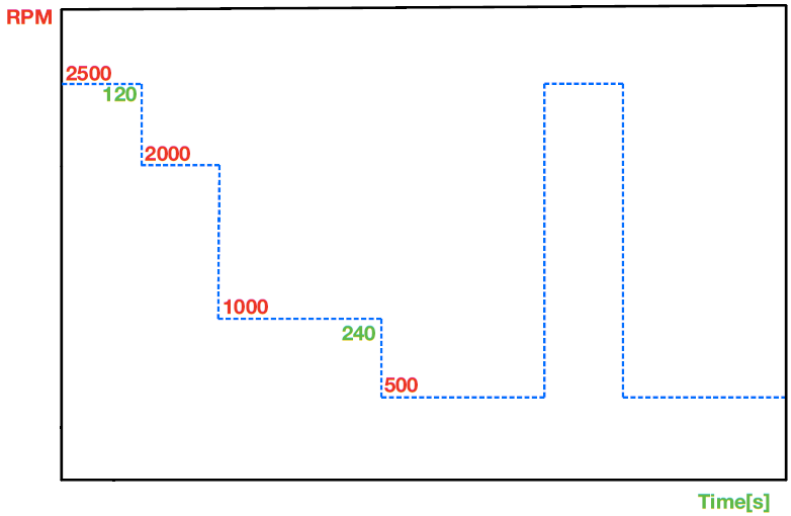

Figure 20: Graphic of RPM profile 2

Two concentration aliquots of Span83 was made; 20ppm and 60ppm. This was done by first making 1 L of 1000 ppm Span83-Exxsol D80 solution (1000ppm). Exxsol D80 (900 mL) was measured in a measuring cylinder (1000 mL) and added to a flask (1 L). Span83 (0.944 g) was measured on analytical balance (Sartorius BP 210 S) into a flask (100 mL). Exxsol D80 (100 mL) was then added to the flask (100 mL) and shaken to mix the surfactant into the oil.

Further, to make Span83-Exxsol D80 solution (20ppm), Exxsol D80 (980 mL) was measured in a measuring cylinder (1000 mL) and added to two flasks (1L). In each flask Span83-Exxsol D80 solution (1000ppm, 20 mL) was added, measured in a measuring cylinder (50 mL).

Experiments were done on seven WCs, seen in Table 1. Experiments started at highest WC. Lowering WC was done by by taking out saline water through the tank outlet into a measuring cylinder. Span83-D80 (20ppm) measured by measuring cylinder was added through the fill hole.

Table 1: Water and oil (Exxsol D80) volumes in seven different WCs

WC	Water [mL]	Oil [mL]
95%	1662.5	87.5
90%	1575	175
85%	1487.5	262.5
20%	350	1400
15%	262.5	1487.5
10%	175	1575
5%	87.5	1662.5

In Table 1 WC volumes was calculated by a fraction calculation. The difference volume of sequential runs were calculated to find the volume of water to be removed and the volume of Exxsol D80 to be added.

After having done seven experiments on seven WCs with Span83-D80 (20ppm) remaining water in the tank was separated from the Span83-D80 (20ppm) by using the tank outlet. Remaining Span83-D80 (20ppm) was measured and collected in two flasks (1 L).

Span83-Exxsol D80 solution (60ppm) was made by removing Span83-D80 (20 ppm, 41 ml) and adding Span83-D80 (1000ppm, 41 mL) to each of two flasks (1 L) containing Span83-D80 (20ppm , 1 L). Then the same seven WC experiments were run, seen in Table 1

Image data was processed both with a SSD-lite neural network, trained on 64 droplet images taken on another camera, and an advanced filtered Hough algorithm. Results of these methods were compared and plotted with DPL evolution data. Figure 21 shows one example of an image processed by the filtered Hough algorithm. 4200 such images were processed over 5 days in this work. Figure 21 also contains a droplet size distribution detected in the image.

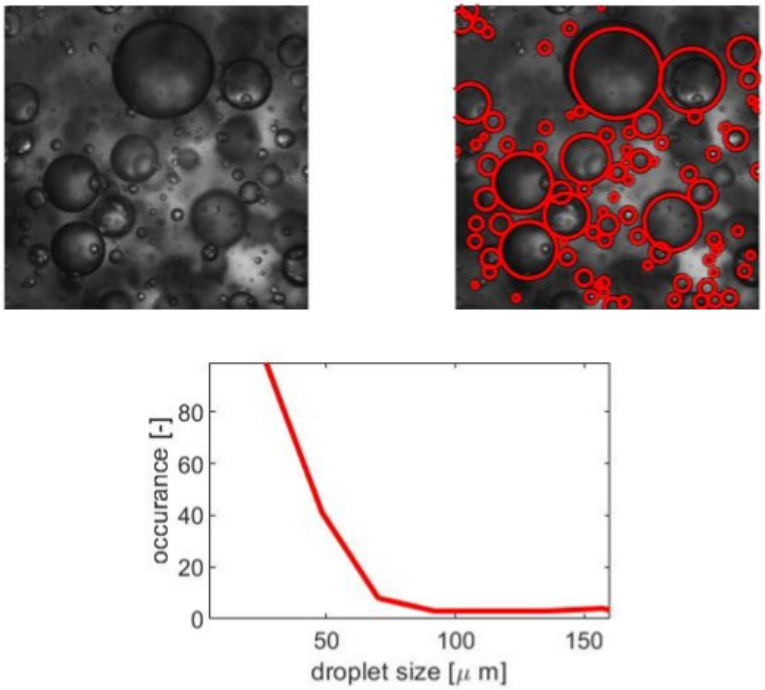

Figure 21: Processed image data

4 Results

4.1 Float device

4.1.1 Initial float device results

The v1 float device testing was done on the first set of 3D-printed devices. Densities and weight of the devices is given in Table 4 in Section B. The two lightest devices would settle on top of the oil, and the two heaviest would settle on the oil-water interface.

For the second set of 3D-printed devices the data logging program was used to measure the height of the devices on the measuring rods. Densities and weight of the devices is given in Table 5 in Section B.

4.1.2 Float device comparison

Comparison of float stability using RPM profile 1 shown in Figure 19 is shown in Figure 22.

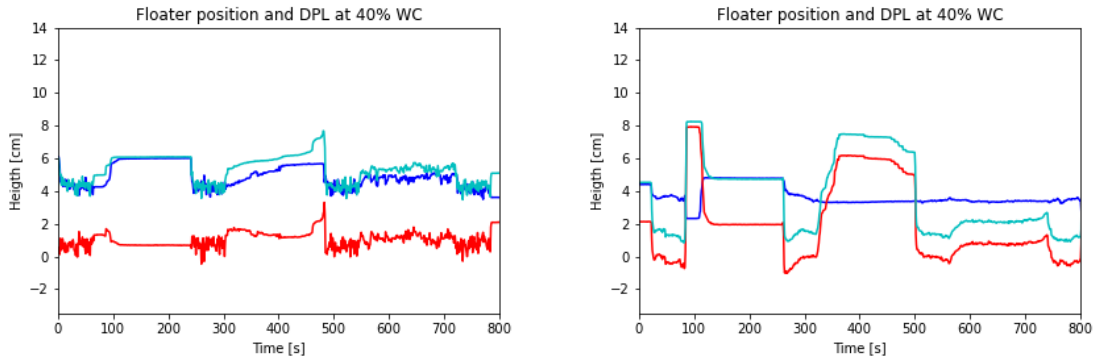

(a) (b)

Figure 22: Float position and DPL plot against time is shown for old floats (a) and new floats (b) at 40% WC no surfactant added. flt_O is shown in cyan flt_W is shown in blue and DPL evolution is shown in red.

4.2 Emulsion stability experiments

4.2.1 Droplet D_{smd} and DPL height from SSD

D_{smd} and DPL height plotted against time for experiments on 85%, 20%, and 10% WC with 20 and 60 ppm span 83 surfactant is given in Figure 23 - Figure 25. DPL height is given as the difference between flt_O and flt_W at the given position. D_{smd} data is gathered from the SSD-lite analysis. RPM profile 2 which is shown in

Figure 20 was used for the experiments. Results for remaining WCs are given in appendix C.1.

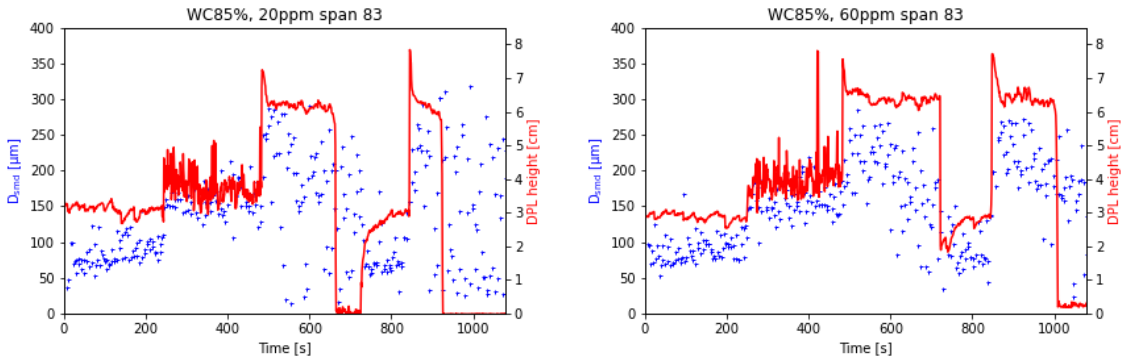

(a) (b)

Figure 23: D_{smd} from SSD and DPL height plot against time in seconds for 20 ppm (a) and 60 ppm (b) span 83 at 85% WC

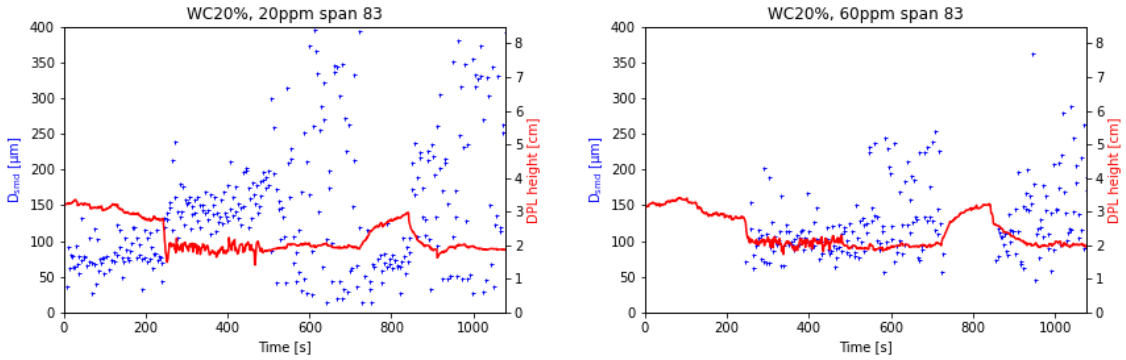

(a) (b)

Figure 24: D_{smd} from SSD and DPL height plot against time in seconds for 20 ppm (a) and 60 ppm (b) span 83 at 20% WC

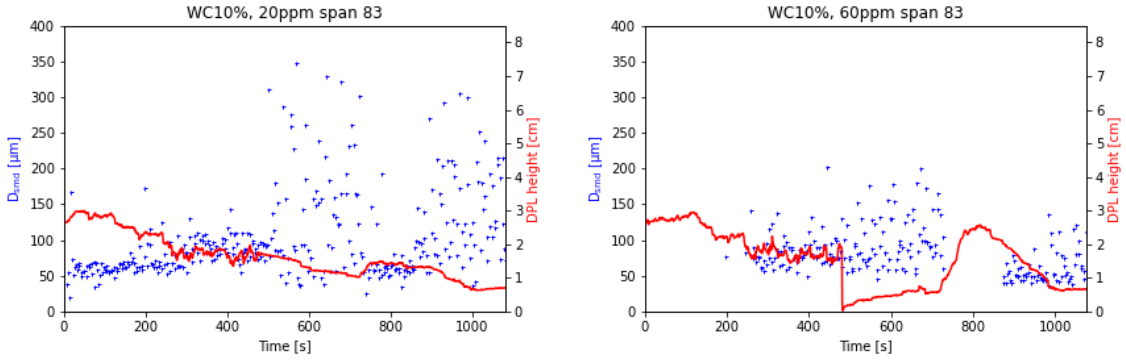

(a) (b)

Figure 25: D_{smd} from SSD and DPL height plot against time in seconds for 20 ppm (a) and 60 ppm (b) span 83 at 10% WC

4.2.2 Droplet D_{smd} and DPL height from Hough

D_{smd} and DPL height plotted against time for experiments on 85%, 20%, and 10% WC with 20 and 60 ppm span 83 surfactant is given in Figure 26 - Figure 28. DPL height is given as the difference between flt_O and flt_W at the given position. D_{smd} data is gathered from the Hough analysis. RPM profile 2 which is shown in Figure 20 was used for the experiments. Results for remaining WCs are given in appendix C.2.

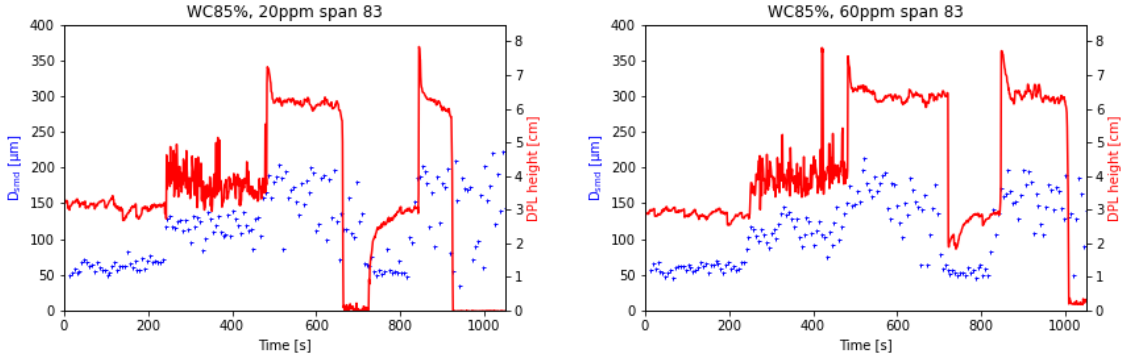

(a) (b)

Figure 26: D_{smd} from Hough and DPL height plot against time in seconds for 20 ppm (a) and 60 ppm (b) span 83 at 85% WC

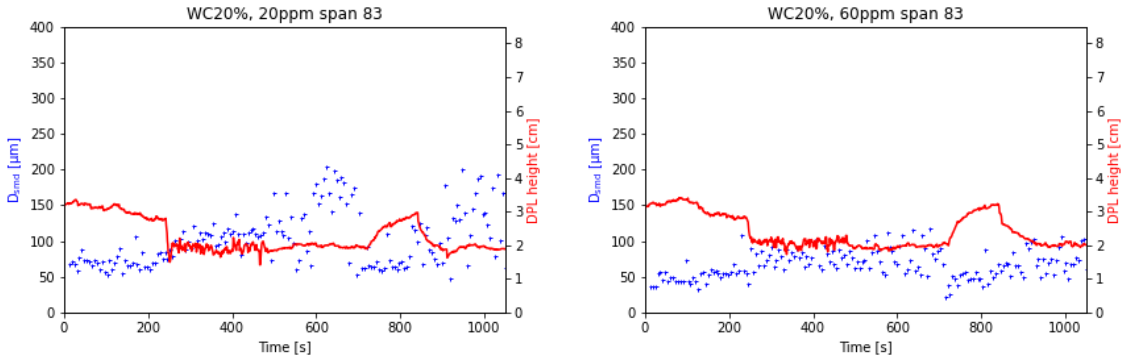

(a) (b)

Figure 27: D_{smd} from Hough and DPL height plot against time in seconds for 20 ppm (a) and 60 ppm (b) span 83 at 20% WC

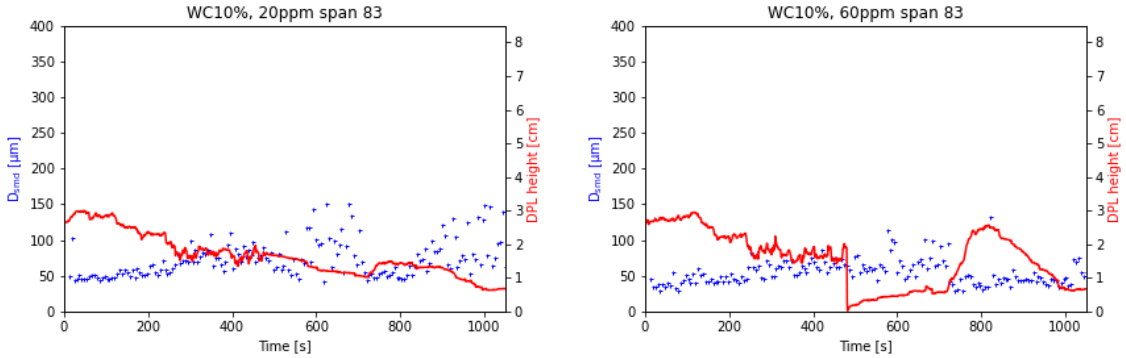

(a) (b)

Figure 28: D_{smd} from Hough and DPL height plot against time in seconds for 20 ppm (a) and 60 ppm (b) span 83 at 10% WC

4.3 SSD-lite and Hough algorithm comparison

Comparison of postproccesed data from both SSD-lite and Hough plotted along each other for 10% WC and both surfactant concentrations is given in Figure 29. Results for remaining WCs are given in appendix C.3.

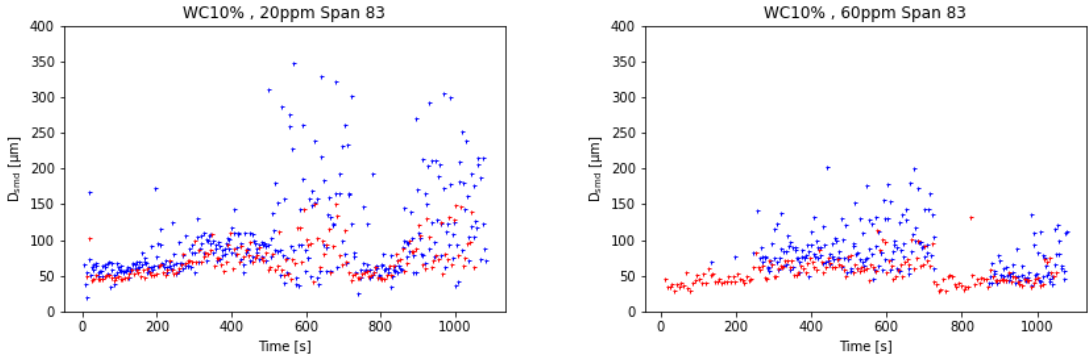

(a) (b)

Figure 29: D_{smd} data from Hough in red and SSD-lite in blue plotted against time in seconds for 20 ppm (a) and 60 ppm (b) span 83 at 10% WC

4.4 Droplet size equilibrium

4.4.1 Kolmogorov length plot

To determine if the emulsion was in the inertial or viscous subrange for each given WC the D_{smd} at equilibrium was plotted against estimated Kolmogorov length from Equation 5. The plot is shown in Figure 30 with shape and color of markers given in Table 2

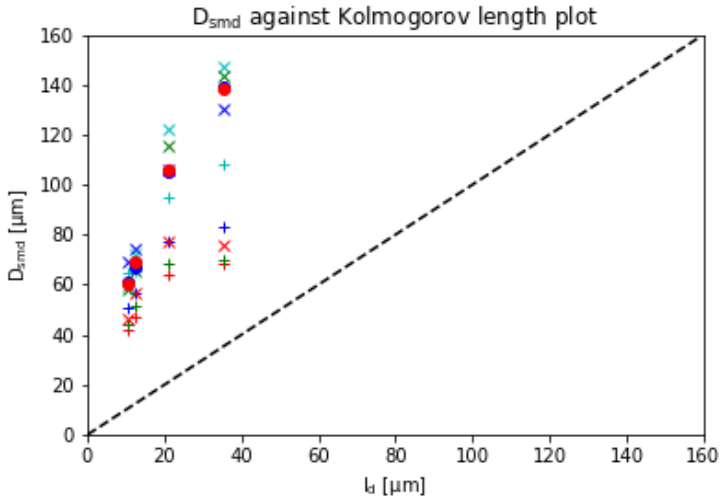

Figure 30: D_{smd} at equilibrium plotted against the Kolmogorov length

Table 2: Kolmogorov plot markers

WC	**20ppm**	**60ppm**
10	Blue +	Red +
15	Cyan +	Green +
20	Blue X	Red X
85	Cyan X	Green X
90	Blue O	Red O

4.4.2 Inertial subrange plot

The interfacial tension for 20 and 60 ppm was estimated by interpolating between the interfacial tension of pure Exxsol D80 and critical micelle concentration of Span83 from Table 7 and Table 8. The interfacial tension that was found to be 40.32 mN/m and 35.24 mN/m respectively. Inertial subrange plots were then fitted for each WC and concentration shown in Figure 31 and Figure 32.

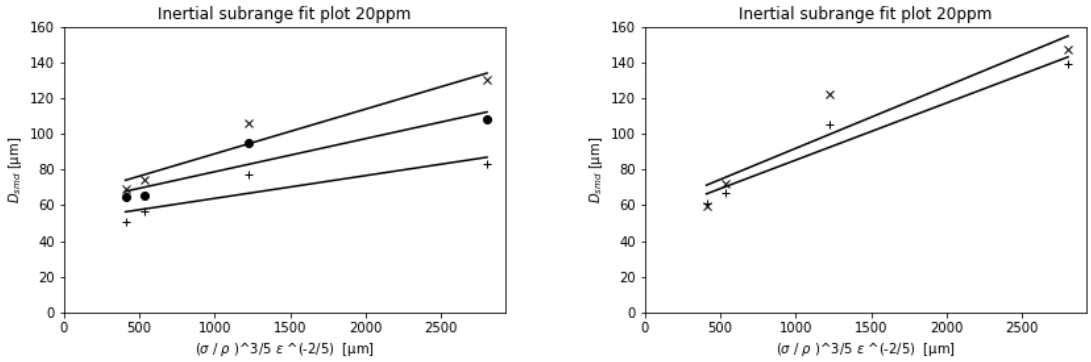

(a) (b)

Figure 31: Inertial subrange plot for WC 10%,15%,20% (a) and 85%,90% (b) at 60 ppm

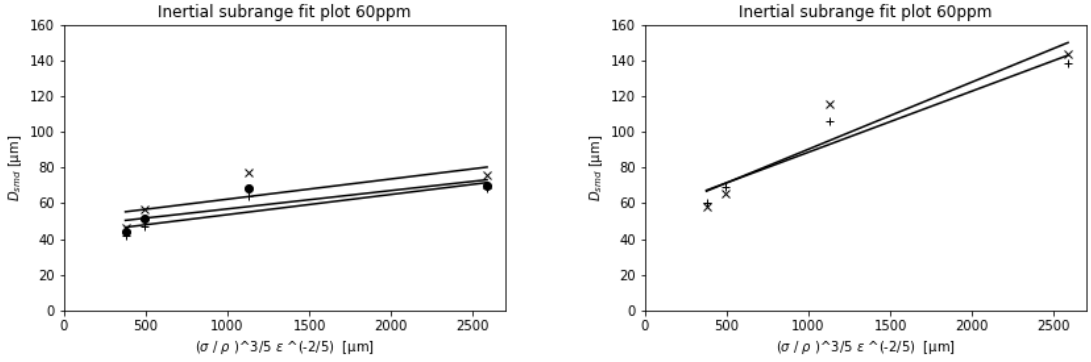

(a) (b)

Figure 32: Inertial subrange plot for WC 10%,15%,20% (a) and 85%,90% (b) at 20 ppm

Inertial coefficient C_i and intercept D_{i0} for all WC for 20 and 60 ppm is given in Table 3. Each value was determined by the slope and intercepts for lines shown in Figure 31 and Figure 32.

Table 3: Inertial coefficients and intercepts

WC	**20ppm** C_i	**60ppm** C_i	**20ppm** D_{i0}	**60ppm** D_{i0}
10	0.0127	0.0113	51.17	42.40
15	0.0185	0.0103	60.30	46.62
20	0.0249	0.0113	63.87	51.64
85	0.0348	0.0376	57.13	52.74
90	0.0319	0.0341	53.42	54.46

5 Discussion

5.1 Development of float device

Development of float system was a trial and error process. Three factors proved to be important: density of floats, material choice and the shape of the floats.

5.1.1 Float density

As seen in Section A.1 the density of the DPL is 857 $\mathrm{kg\,m^{-3}}$. This is based on a densest spherical packing model, which is disputed for the DPL density[31]. In a water-in-oil emulsion water droplets will in an ideal scenario form this dense spherical packing, but because droplets are elastic and will flocculate and coalesce the DPL might vary in density. It is hard to estimate DPL density, it likely is dependent on droplet dynamics. It might be that there is a density gradient through the DPL, seeing that droplet size varies throughout the layer. It could also be plausible that the DPL density is dependent on WC. From video microscope images in Results it can be seen that WC affects droplet size. The addition of surfactants will also affect droplet dynamics, which in turn might affect DPL density, as droplet dynamics might disrupt dense spherical packing.

Although density of the DPL is uncertain, some literature points to the dense spherical packing model[31]. Therefor it was thought that two floats should be made considering DPL density of 857$\mathrm{kg\,m^{-3}}$. One float with a density smaller than 857$\mathrm{kg\,m^{-3}}$, but smaller than that of Exxsol D80. This would therefor float on the oil-DPL interface($\mathrm{flt_O}$). A second float would have a density larger than 857$\mathrm{kg\,m^{-3}}$, but smaller than that of saline water, so to float on the DPL-water interface($\mathrm{flt_W}$).

Mostly the optimal density within the above mentioned intervals were achieved through trial and error. From know volume in SoldiWorks 2021 weight of the v1 floats was calculated from target density. This weight was then input in a 3D printing software. Because of inaccuracies in 3D printing there was a challenge in producing the right density of the floats. Although 3D printing is considered a method good for prototyping, as it is able to provide a quick turnaround in production, for this instance of simply adjusting the density of floats it proved time consuming and inaccurate. The technique also results in rough surfaces and pours a product which is discussed later. The density of the final iteration of floats was adjusted by adding some mass or taking out some mass, then observe float performance. The floats had a usable density at 941$\mathrm{kg\,m^{-3}}$ for $\mathrm{flt_W}$and 827$\mathrm{kg\,m^{-3}}$ for $\mathrm{flt_O}$. Tap water was added to get these densities. This way of adjusting the density of the floats was quick and more accurate than 3D printing.

5.1.2 Material choice

The material used for v1 floats was ONYX. The nylon reinforced by micro carbon fibers was chosen for its chemical resistant properties. The 3D printed ONYX was thought to absorb water, both because of nylons water absorbing properties and because of the porous nature of 3D printed parts. The former might be solved by coating the 3D printed floats with some water replant spray[41]. The later could be combated by using some other 3D printing technique, such as SLA or SLS[35]. Because of the rough surface of the floats droplets would be observed to adhere to them. It was determined that this was water droplets as they would fall down into the water layer after a while. The v2 floats were machined out of PEEK, which made a smoother surface and a higher level of precision than the MarkForge 3D printer used. PEEK was also chosen for its chemical resistant properties. Both High density polyethylen (HDPE) and aluminum was considered. This material was thought suited for the purpose because of the low density, but was determined to have low resistance to petroleum products such as Exxsol D80.

5.1.3 Float design

The shape and size of the v1 floats was designed to have good hydrodynamic property and to fit the space constraints by the stirred tank and the MMRs. These could more easily be made smaller than the v2 floats, because of the nature of 3D printing and because of the simplicity of the design. It was thought that a smaller design would be less susceptible to turbulence in the tank, because of its smaller surface area, and would fit the constraints of the tank better. The challenge of the v2 float design is that it is a complicated design made out of a high density material, in PEEK. Some of the parts has to be completely solid, which weighs the float down. To keep the float light it was made larger, so to add air volume, without adding much material volume. The v2 floats is a more complicated design. Because the parts are completely solid it was designed with a void space to achieve a density lower than that of Exxsol D80. This void had to be large enough to get the right density, therefor the floats would also have to have a minimum size. The height of the floats led to challenge which affected how it was possible to measure DPL height. It was observed that when the DPL was at its largest height it would push the float against the top-plate of the tank. The float would not fall with the DPL before the DPL height had reached the bottom of the float, this is illustrated in Figure 33. Because of this it was not possible to measure the top 3-4 cm of the DPL evolution.

This problem could be solved by making a shorter float design. This could either be done by making the float shorter and increasing the diameter or by using a material with lower density. In the comparison test of floats shown in Section 4.1.2 it can be seen that the larger float is less susceptible to forces in the turbulent flow. This was unexpected and the cause was not determined, but could be because the larger floats are heavier. There was lesser amount of water droplets observed gathering on the v2 floats, but there were observed droplets gathering around the screws on the float top. One simple fix to this was to turn the floats so that the screws pointed downwards.

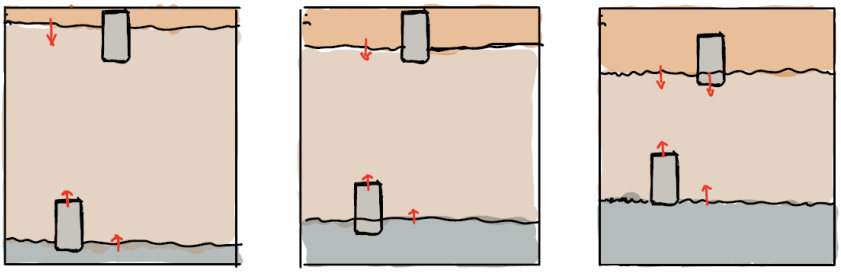

Figure 33: Illustrating drawback of a tall float design. Arrows indicating movement of DPL height. When DPL reaches the bottom of flt_O, flt_Ostarts to move.

5.2 Emulsion monitoring

5.2.1 Droplet D_{smd} and DPL height

Generally changes in the height difference between the floats (DPL height) and the D_{smd} coincide with the changes in RPM from Figure 20. The difference in DPL evolution is also fairly similiar for both 20 ppm and 60 ppm Span 83. Some differences are present however. As seen in Figure 26 (a) the DPL height drops to 0 cm at around 650 s, while (b) drops at around 700 s to a DPL height of about 2 cm. The height in (b) at 700 s also coincides with the height of (a) at the same time with both heights rising to about 3 cm at the same pace from that point until around 850 s. This indicates that the float most likely got held back or stuck for around 50 s after the increase from 500 to 2500 RPM before it sank to the expected position. This is also shown for the drop around 900 s in (a) which happens at around 1000 s in (b).

D_{smd} between 20 ppm and 60 ppm are fairly similar at 1000 RPM and over. This can be seen in Figure 26-Figure 28 compared to the RPM profile from Figure 20. This is not the case however for 500 RPM where there is greater spread as shown in Figure 28 (a) at around 600 s than in (b). Some difference in droplet size also seems to occur in Figure 27 at this time with higher droplet size in (a) than in (b).

5.2.2 SSD-lite and Hough comparison

As seen in Figure 29, 41 and 43 (b) the ssd-lite analysis did not produce D_{smd} data at 2500 rpm for these experiments. This is most likely due to the image-sets for these runs being quite dark and so the ssd-lite network could not reliably detect droplets in these regions as the droplet size decreased. The fact that the network was trained on an image-set from another camera could also make detection harder, especially at such small droplet size.

Generally shown in the plots the SSD analysis seems to estimate larger droplet sizes than those estimated from Hough. At some points, especially around speeds of 500 rpm it can be seen that the spread of estimated droplet sizes is significantly higher than that of those estimated by Hough. An example of this can be seen in Figure 29 (a) where the highest estimated D_{smd} values is around 300 µm while the lowest values are around 70 µm with the rest being fairly spread inbetween. This however is not the case in the Hough analysis where the estimated D_{smd} is much less spread and has fewer outliers.

5.2.3 Kolmogorov length plot

As seen in Figure 30 all D_{smd} measurements at equilibrium were larger than the Kolmogorov length indicating that the measurements were in the inertial subrange. This yields similiar results to a recent work where exxsol D80 WC from 5% to 95% all had higher D_{smd} than the Kolmogorov length for 1000,2000, and 3000 RPM [8]. However in these experiments no surfactant was added. On the other hand the kolmogorov length plot from another work done on crude oil variations show WCs lesser than 20% to belong to the viscous subrange [5]. This is likely due to the crude oil variations used having higher viscosity than that of Exxsol D80 [5]. Another factor could be the increased effect of the surfactants present in crude oil could have a higher effect on the viscosity than that of Span83.

5.2.4 Inertial subrange

Inertial coefficients in Table 3 indicates the o/w emulsions for both 20 and 60 ppm Span83 were most stable. This is because the coefficients for 85% and 90% WC are around 0.033 and the coefficients for 10% to 20% are around half of that around 0.018 for 20 ppm, and similarly 0.035 and 0.011 for 60 ppm. The intercepts of 20 ppm were higher for all but 90% WC than that of 60 ppm. This would imply that the droplets at 20 ppm concentration were more rigid and stable than 60 ppm. For 20 ppm the droplet intercept increases from high and low WC towards 20% with a value of 63.87 µm. For 60 ppm the droplet intercept steadily rises from 10% WC at 42.40 µm to 90% WC at 54.46 µm. These values however might have some form of error since both the power input and interfacial tensions were estimated. Especially the interfacial tension which was estimated by linear interpolation. This however would not likely affect the trends seen here but rather the values themselves.

5.3 Other sources of error

During the development and testing of the floats there would often be some form of viscous contaminant building up after every couple of runs. The contaminant did not have a large impact on the floaters most of the time, but sometimes it would lead to the floater settling at unusual positions or getting stuck. After some examination it was noted that the rubber packing ring used to seal the tank and lid was slowly deteriorating in contact with the oil. After this a new ring of oil resistant Viton plastic was ordered for the tank. Although this did not affect the results presented here, it did slow down the process of getting the floaters to work consistently by some time.

As experiments with the probe commenced it was noticed that some white matter was starting to build up in the oil. This matter however did not affect the floaters and did not seemingly affect the quality of the droplet images at first. There is however a chance that this could have contributed to some images in Figure 24, 25 and 36 (b) being darker as the oil was very opaque towards the end. As other sources of contamination had already been removed and the equipment was thoroughly cleaned before the experiments a direct cause for the buildup is yet to be determined, but it was thought that it may be either salt from the saline water or something polar binding with the span 83 in the oil.

5.4 Further work

Below is list with som pointers and implementations that could be done to the system to increase its overall performance:

Adjusting the light source for the probe if possible. Some images especially at low WC would come out hard to see. This also made it hard to adjust the focus of the probe during high RPM, even more so since the Linux computer used had a relatively dark screen with bad viewing angles.

Using the torque sensor together with the probe and float system would give a better estimate of the power input into the system.

Using metal baffles instead of 3D-printed ones would help with consistency. The current baffles bend significantly, especially under high RPM. A stabilisation ring at or close to the bottom of the baffles should also be included to further increase stability.

Hole perforated pipes should be tested further, ideally in metal as our runs did not produce results due to them being to flimsy and hard to fit correctly.

If hole perforated pipes yield results indicating smaller floats can be used, a shorter iteration could be made. This could be made similar to our design but with thinner walls to compensate for the reduced height. There is a possibility this could be done by using some type of metal but corrosion resistance and droplet sticking must be a consideration.

6 Conclusion

A custom video microscope camera probe and float system was developed and used to measure droplet size distribution and DPL evolution in a stirred tank cell system. This system was further developed from earlier work at SINTEF Industry. Experiments were done on seven different WC ranging from 5% - 95% with 20 and 60 ppm Span83 in Exxsol D80. Efficiency of the float system was compared between a new and an older iteration. The newer iteration was found to work better, but still had some limitations. SSD-lite and Hough post processing was compared with data gathered from the experiments. Equilibrium droplet sizes was plotted against the Kolmogorov length scale and the emulsion was determined to be in the inertial subrange at all values. Inertial subrange plots were fitted for each WC and concentration combination. The inertial coefficient and intercepts were determined from the plots.

References

[1] F. Goodarzi and S. Zendehboudi. 'A Comprehensive Review on Emulsions and Emulsion Stability in Chemical and Energy Industries'. In: *The Canadian Journal of Chemical Engineering* 97 (Nov. 2018). DOI: 10.1002/cjce.23336.

[2] J.R. Becker. *Crude oil waxes, emulsions and asphaltenes*. PennWell Publishing Company, 1997.

[3] B. Panjwani. *IMPOSE - Improved Separator Design through Dense Packed Layer Extraction and Treatment*. URL: https://www.sintef.no/en/projects/2018/impose-improved-separator-design-through-dense-packed-layer-extraction-and-treatment/ (visited on 16th May 2022).

[4] P. Becher. *Emulsions Theory and Practice*. Oxford University Press, Inc, 2001.

[5] A. Patil et al. 'Crude oil characterization with a new dynamic emulsion stability technique'. In: *Fuel* 290 (Apr. 2021), p. 120070. DOI: 10.1016/j.fuel.2020.120070.

[6] C. J. Geankoplis. *Transport Processes and Separation Process Principles*. Pearson Education Limited, 1993.

[7] S. Kokal. 'Crude-Oil Emulsions: A State-Of-The-Art Review'. In: *SPE Production & Facilities* 20.01 (2005), pp. 5–13. DOI: 10.2118/77497-PA.

[8] A. Patil, B. Sægrov and B. Panjwani. 'Advanced deep learning for dynamic emulsion stability measurement'. In: *Computers & Chemical Engineering* 157 (Nov. 2021), p. 107614. DOI: 10.1016/j.compchemeng.2021.107614.

[9] M. Zlokarnik. *Stirring - Theory and Practice*. Wiley-VCH, 2001.

[10] P. M. Doran. *Bioprocess Engineering Principles*. Academic Press, 2013.

[11] User Echis - Wikipedia. *Batch Reactor*. URL: https://commons.wikimedia.org/wiki/File:Batch_reactor.2.jpg (visited on 18th May 2022).

[12] R. A. Serway and J. W. Jewett. *Physics for Scientists and Engineers*. Brooks Cole, 2003.

[13] P. P. Urone and R. Hinrichs. *Physics*. OpenStax, 2020.

[14] CALT sensors. *What Is Torque Sensor? — How Does It Work?* URL: https://caltsensor.com/what-is-torque-sensor-how-does-it-work/ (visited on 11th Apr. 2022).

[15] Piezodirect. *What Are Piezoelectric Sensors?* URL: https://piezodirect.com/piezoelectric-sensor/ (visited on 11th Apr. 2022).

[16] W. L. McCabe and J. C. Smith. *Unit Operations of Chemical Engineering*. McGraw Hill, 1993.

[17] M. Abidin, A. Abdul Raman and M. Nor. 'Review on Measurement Techniques for Drop Size Distribution in a Stirred Vessel'. In: *Industrial & Engineering Chemistry Research* 52 (Nov. 2013), pp. 16085–16094. DOI: 10.1021/ie401548z.

[18] J. Boxall et al. 'Measurement and Calibration of Droplet Size Distributions in Water-in-Oil Emulsions by Particle Video Microscope and a Focused Beam Reflectance Method'. In: *Industrial & Engineering Chemistry Research - IND ENG CHEM RES* 49 (Dec. 2009). DOI: 10.1021/ie901228e.

[19] Teledyne DALSA. *CCD vs. CMOS*. URL: https://www.teledynedalsa.com/en/learn/knowledge-center/ccd-vs-cmos/ (visited on 18th Apr. 2022).

[20] D.H. Ballard. 'Generalizing the Hough Transform to Detect Arbitrary Shapes'. In: *Pattern Recognition* 13 (Dec. 1987), pp. 111–122. DOI: 10.1016/0031-3203(81)90009-1.

[21] A. Patil et al. 'Development of an advanced imaging technique for dynamic emulsion stability'. In: *Chemical Engineering Journal* 322 (Mar. 2017). DOI: 10.1016/j.cej.2017.02.156.

[22] J. Canny. 'A Computational Approach To Edge Detection'. In: *Pattern Analysis and Machine Intelligence, IEEE Transactions on* PAMI-8 (Dec. 1986), pp. 679–698. DOI: 10.1109/TPAMI.1986.4767851.

[23] jun-devp Medium Blog. *[CV] 6. Structure Extraction with Hough Transform (line, circle)*. URL: https://medium.com/jun94-devpblog/cv-6-structure-extraction-with-hough-transform-line-circle-aaf8be62f169 (visited on 28th Apr. 2022).

[24] IBM Cloud Education. *Neural Networks*. URL: https://www.ibm.com/cloud/learn/neural-networks (visited on 19th Apr. 2022).

[25] IBM Cloud Education. *Machine Learning*. URL: https://www.ibm.com/cloud/learn/machine-learning (visited on 21st Apr. 2022).

[26] IBM Cloud Education. *Convolutional Neural Networks*. URL: https://www.ibm.com/cloud/learn/convolutional-neural-networks (visited on 19th Apr. 2022).

[27] Z. Zhao et al. 'Object Detection With Deep Learning: A Review'. In: *IEEE Transactions on Neural Networks and Learning Systems* 30.11 (2019), pp. 3212–3232. DOI: 10.1109/TNNLS.2018.2876865.

[28] ArcGIS Developer. *How single-shot detector (SSD) works?* URL: https://developers.arcgis.com/python/guide/how-ssd-works/ (visited on 12th May 2022).

[29] Tensor Flow. *TensorFlow Lite Model Maker*. URL: https://www.tensorflow.org/lite/guide/model_maker (visited on 12th May 2022).

[30] J. Yi et al. 'Fast Neural Cell Detection Using Light-Weight SSD Neural Network'. In: *2017 IEEE Conference on Computer Vision and Pattern Recognition Workshops (CVPRW)* (2017), pp. 860–864. DOI: 10.2118/77497-PA.

[31] S. Keleşoğlu et al. 'Rheological properties of highly concentrated dense packed layer emulsions (w/o) stabilized by asphaltene'. In: *Journal of Petroleum Science and Engineering* 126 (Feb. 2015). DOI: 10.1016/j.petrol.2014.11.031.

[32] ABB. *A dozen ways to measure fluid level*. URL: https://new.abb.com/products/measurement-products/level/a-dozen-ways-to-measure-fluid-level (visited on 21st Apr. 2022).

[33] T. Calkins, A. Flatau and M. Dapino. 'Overview of Magnetostrictive Sensor Technology'. In: *Journal of Intelligent Material Systems and Structures - J INTEL MAT SYST STRUCT* 18 (Oct. 2007), pp. 1057–1066. DOI: 10.1177/1045389X06072358.

[34] S. Ligon et al. 'Polymers for 3D Printing and Customized Additive Manufacturing'. In: *Chemical Reviews* 117 (July 2017). DOI: 10.1021/acs.chemrev.7b00074.

[35] Form Labs. *3D Printing Technology Comparison: FDM vs. SLA vs. SLS*. URL: https://formlabs.com/blog/fdm-vs-sla-vs-sls-how-to-choose-the-right-3d-printing-technology/ (visited on 27th Apr. 2022).

[36] Stanley Machining. *CNC Machining vs 3D Printing*. URL: https://www.stanleymachining.com/post/cnc-machining-vs-3d-printing (visited on 27th Apr. 2022).

[37] Form Labs. *What Does Resolution Mean in 3D Printing?* URL: https://formlabs.com/blog/3d-printer-resolution-meaning/ (visited on 27th Apr. 2022).

[38] MakerBot. *EVERYTHING YOU NEED TO KNOW ABOUT NYLON 3D PRINTING*. URL: https://www.makerbot.com/stories/design/nylon-3d-printing/ (visited on 27th Apr. 2022).

[39] MarkForge. *Material Datasheet. Composits; Onyx, Onyx FR, Onyx ESD, Nylon*. URL: https://www-objects.markforged.com/craft/materials/CompositesV5.2.pdf (visited on 27th Apr. 2022).

[40] P. Patel et al. 'Mechanism of thermal decomposition of poly(ether ether ketone) (PEEK) from a review of decomposition studies'. In: *Polymer Degradation and Stability - POLYM DEGRAD STABIL* 95 (May 2010), pp. 709–718. DOI: 10.1016/j.polymdegradstab.2010.01.024.

[41] DuPont. *DuPont™ Silicone Lubricant with Teflon® fluoropolymer - Aerosol*. URL: https://etc.engineering.uiowa.edu/sites/etc.engineering.uiowa.edu/files/9508.pdf (visited on 14th May 2022).

[42] ExxonMobile. *Safety Data Sheet*. URL: https://logistikportalen.fmv.se/tjansterprodukter/sdb/SDB_M07nr/M0702-013015_EXXSOL%5C%20D80_A1.pdf (visited on 16th May 2022).

[43] ExxonMobile. *Exxsol D80 - Dearomatized fluid*. URL: https://www.pure-chemical.com/msds/Exxsol%5C%20D80.pdf (visited on 16th May 2022).

[44] CRODA. *SPAN 83 PHARMA-LQ-(MV)*. URL: https://msds.crodadirect.com (visited on 18th May 2022).

Appendix

A Calculations

A.1 Density calculations of the DPL for water-in-oil emulsion

$$\rho_{D80} = 798\frac{kg}{m^3}$$
$$\rho_{salinewater} = 1025\frac{kg}{m^3}$$

Densest sphere packing ratio in water-in-oil dispersion: 74% oil and 26% water

$$\rho_{DPL} = \rho_{D80} * 0.74 + \rho_{salinewater} * 0.26 = 857\frac{kg}{m^3}$$

A.2 Density calculation of the DPL for oil-in-water emulsion

Densest sphere packing ratio in oil-in-water dispersion: 26% oil and 74% water

$$\rho_{DPL} = \rho_{D80} * 0.26 + \rho_{salinewater} * 0.74 = 966\frac{kg}{m^3}$$

A.3 Density calculations for v1 float device

$$\rho_{D80} = 798\frac{kg}{m^3}$$
$$\rho_{DPL} = 857\frac{kg}{m^3}$$
$$\rho_{salinwater} = 1025\frac{kg}{m^3}$$

$$\rho_{fltO} = \frac{\rho_{D80} + \rho_{DPL}}{2} = 827\frac{kg}{m^3}$$
$$\rho_{fltW} = \frac{\rho_{saltWater} + \rho_{DPL}}{2} = 941\frac{kg}{m^3}$$

A.4 Density calculation of v2 float device

$$V_{cyl1} = 50mm * \pi * (11.5mm)^2 = 20773.8mm^3$$
$$V_{cyl0} = 50mm * \pi * (5.5mm)^2 = 4751mm^3$$
$$V_{flt} = V_{cyl1} - V_{cyl0} = 16022.1mm^3 = 1.602 * 10^{-5}m^3$$
$$m_{flt} = 15.35g = 1.535 * 10^{-2}kg$$
$$\rho_{flt} = \frac{m_{flt}}{V_{flt}} = 958\frac{kg}{m^3}$$

A.5 Saline water calculation

Calculating the amount of salt needed in 1 L of water to get a 35 ppm saline water solution

$$3.5\% * 1000g_{water} = 35gsalt$$

$$35g * 5 = 175g$$

A.6 Span 83 calculations

Calculating the amount of Span 83 needed in 1 L of Exxsol D80 to get a 1000ppm Exxsol D80 - Span 83 solution.

$$0.1\% * 1000g_{water} = 1gSpan83$$

$$V_1 = \frac{c_2 * V_2}{c_1}$$

$$V_1 = \frac{20ppm * 2000mL}{1000ppm} = 40mL$$

B Flotation device properties

Table 4: Weight and density of the first four flotation devices 3D-printed with Onyx nylon material.

Flotation device	Weight [g]	Density [kg/m3]
1	1.569	751.4
2	1.775	850.25
3	1.740	833.25
4	1.408	674.3

Table 5: Weight and density of the six new flotation devices 3D-printed with Onyx nylon material. Unable to find values for device 6

Flotation device	Weight [g]	Density [kg/m3]
1	1.908	913.5
2	1.689	808.7
3	1.862	891.6
4	1.951	934.3
5	1.932	925.2
6	N/A	N/A

C More results

C.1 More SSD analysis plots

D_{smd} and DPL height plotted against time for experiments on 95%, 90%, 15% and 5% WC with 20 and 60 ppm span 83 surfactant is given in Figure 34 - Figure 37. DPL height is given as the difference between flt_O and flt_W at the given position. D_{smd} data is gathered from the SSD-lite analysis. RPM profile 2 which is shown in Figure 20 was used for the experiments.

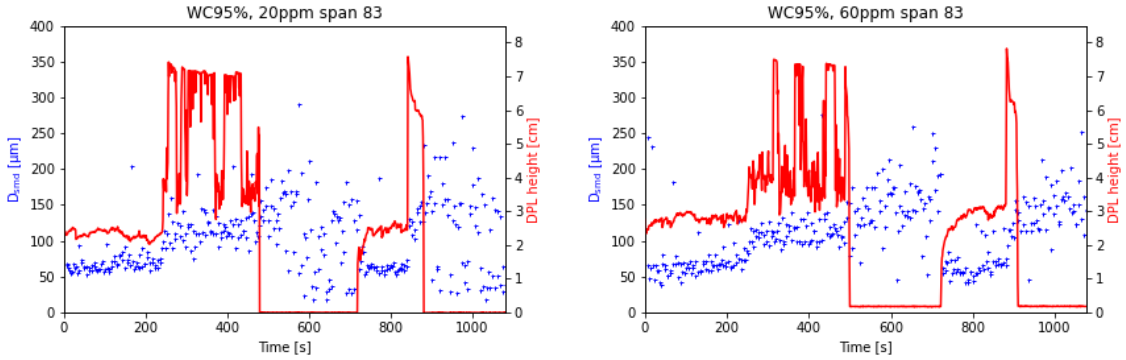

(a) (b)

Figure 34: D_{smd} from SSD and DPL height plot against time in seconds for 20 ppm (a) and 60 ppm (b) span 83 at 95% WC

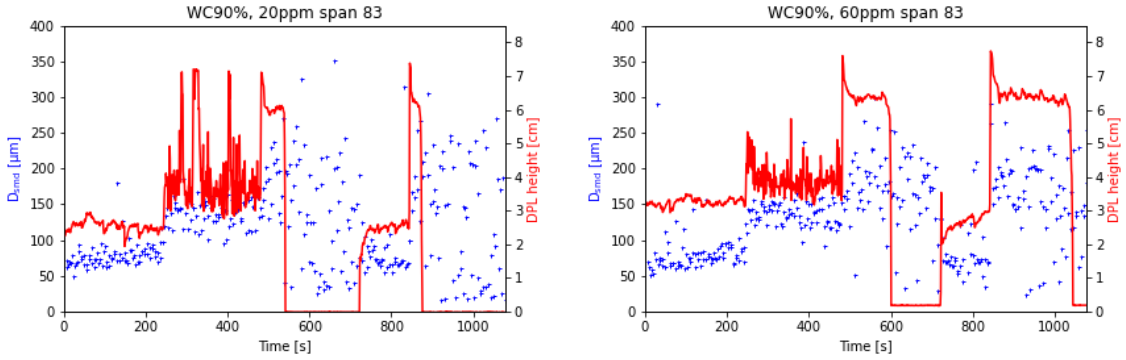

(a) (b)

Figure 35: D_{smd} from SSD and DPL height plot against time in seconds for 20 ppm (a) and 60 ppm (b) span 83 at 90% WC

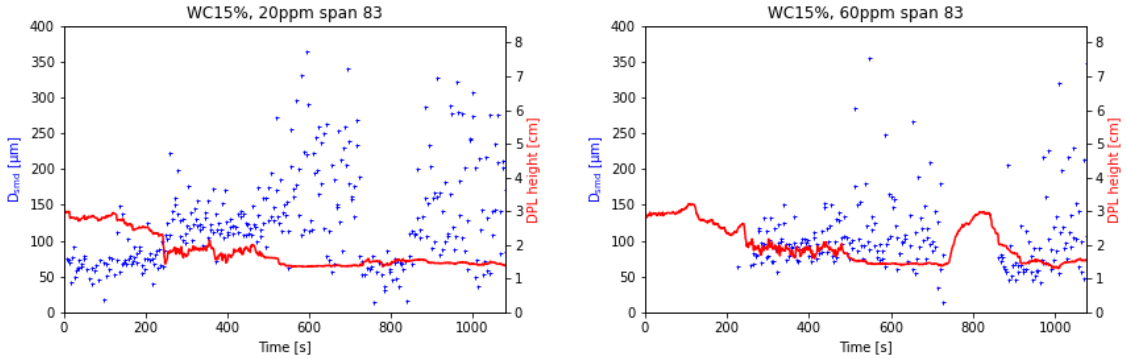

(a) (b)

Figure 36: D_{smd} from SSD and DPL height plot against time in seconds for 20 ppm (a) and 60 ppm (b) span 83 at 15% WC

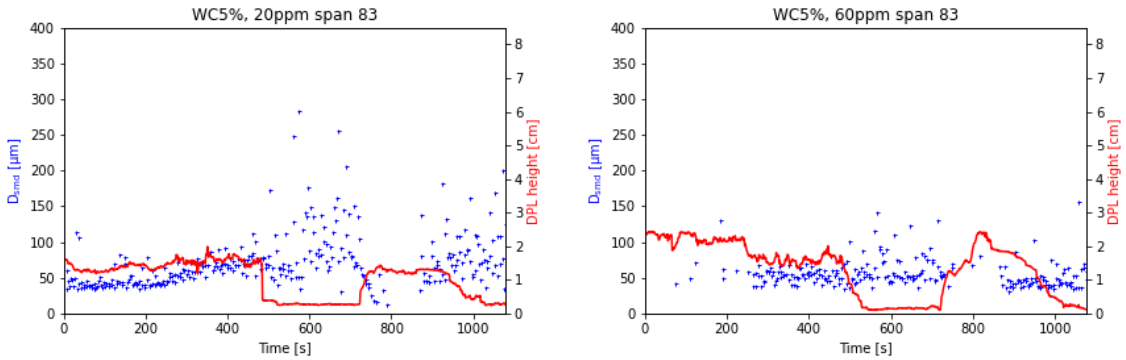

(a) (b)

Figure 37: D_{smd} from SSD and DPL height plot against time in seconds for 20 ppm (a) and 60 ppm (b) span 83 at 5% WC

C.2 More Hough analysis plots

D_{smd} and DPL height plotted against time for experiments on 90%, and 15% WC with 20 and 60 ppm span 83 surfactant is given in Figure 38 - Figure 39. DPL height is given as the difference between flt_O and flt_W at the given position. D_{smd} data is gathered from the Hough analysis. RPM profile 2 which is shown in Figure 20 was used for the experiments. Due to time constraints data from 95% and 5% WC did not get processed.

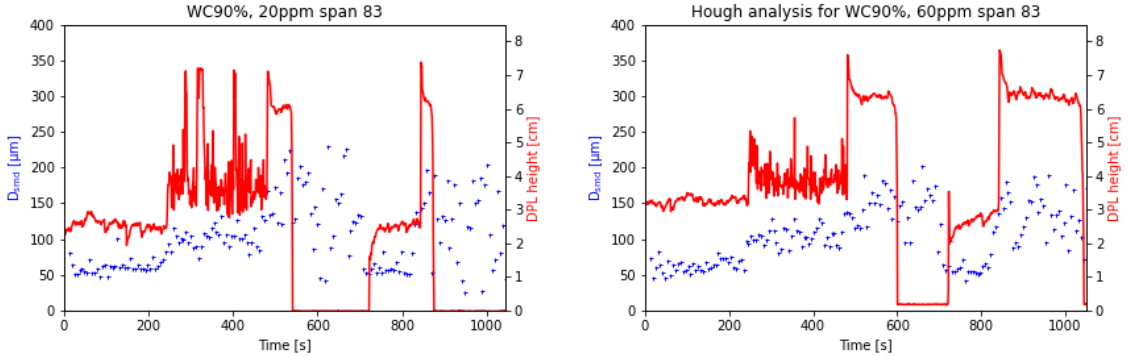

(a) (b)

Figure 38: D_{smd} from Hough and DPL height plot against time in seconds for 20 ppm (a) and 60 ppm (b) span 83 at 90% WC

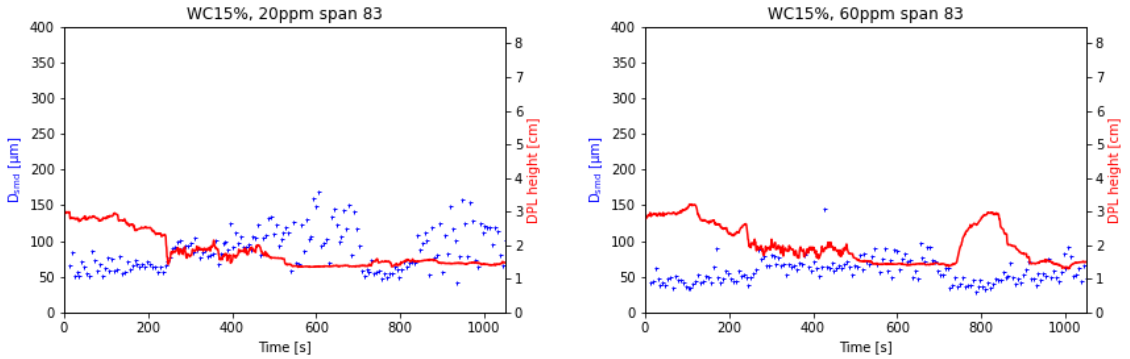

(a) (b)

Figure 39: D_{smd} from Hough and DPL height plot against time in seconds for 20 ppm (a) and 60 ppm (b) span 83 at 15% WC

C.3 More SSD-Lite and Hough comparisons

Comparison of postproccesed data from both SSD-lite and Hough plotted together for 15% - 90% WC and both surfactant concentrations is given in Figure 40-Figure 43.

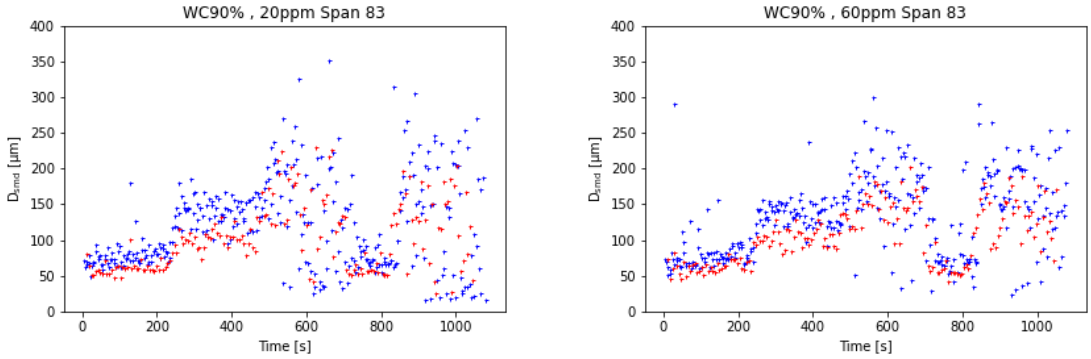

(a) (b)

Figure 40: D_{smd} data from Hough in red and SSD-lite in blue plotted against time in seconds for 20 ppm (a) and 60 ppm (b) span 83 at 90% WC

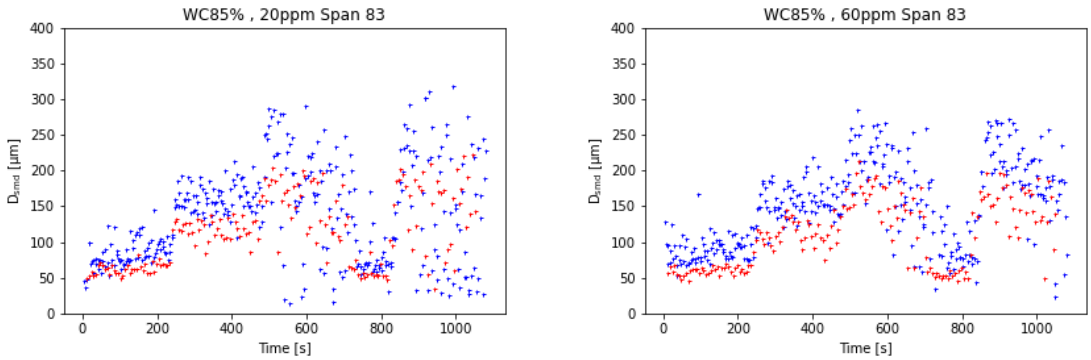

(a) (b)

Figure 41: D_{smd} data from Hough in red and SSD-lite in blue plotted against time in seconds for 20 ppm (a) and 60 ppm (b) span 83 at 85% WC

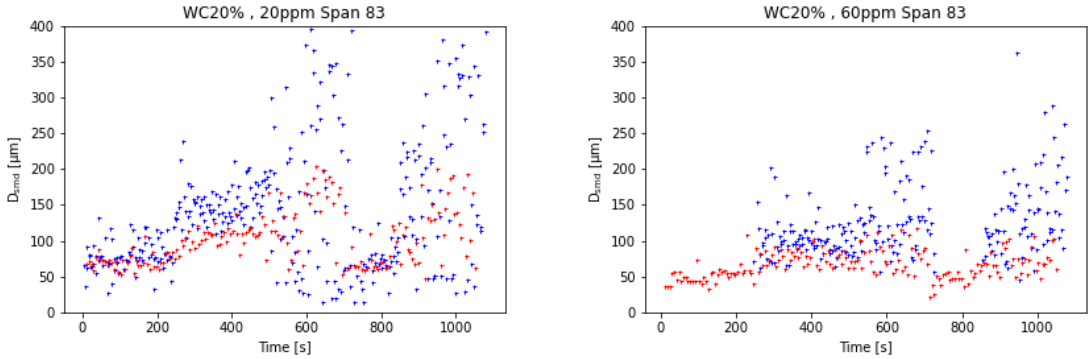

(a) (b)

Figure 42: D_{smd} data from Hough in red and SSD-lite in blue plotted against time in seconds for 20 ppm (a) and 60 ppm (b) span 83 at 20% WC

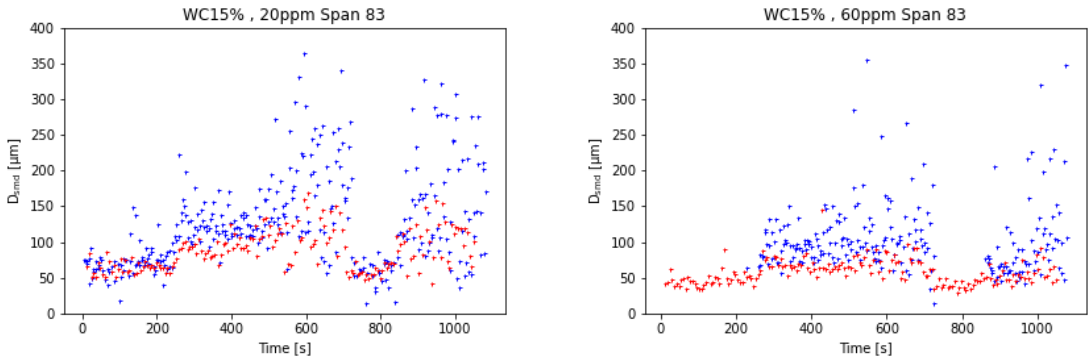

(a) (b)

Figure 43: D_{smd} data from Hough in red and SSD-lite in blue plotted against time in seconds for 20 ppm (a) and 60 ppm (b) span 83 at 15% WC

D Information Chemicals

D.1 MSDS Exxsol D80

Table 6: Hazard statements and Precautionary Statements for Exxsol D80[42]

Hazard statement index[42]	**Hazard statement**
H304	May be fatal if swallowed and enters airways
EUH066	Repeated exposure may cause skin dryness or cracking
Precautionary Statement Index	**Precautionary Statements**
P210	Keep away from heat, hot surfaces sparks, open flames and other ignition sources. No smoking
P280	Wear protective gloves and eye / face protection
P301+P310	IF SWALLOWED: Immediately call POISON CENTRE or doctor/physician
P311	Do NOT induce vomiting
P370 + P378	In case of fire: Use water fog, foam, dry chemicals or carbon dioxode (CO2)
P403 + P235	Store in a well-ventilated place. Keep cool.
P405 + P235	Store locked up.

D.2 Properties Exxsol D80

Table 7: Properties of Exxsol D80

Description[43]	Dearomatized fluid
Density[43]	798 kg/m3
Viscosity[43]	1.68 mm2/sec
IFT[8]	42.87 $\mathrm{m\,N\,m^{-1}}$

D.3 MSDS Span 83

No Hazard/Precautionary statements

D.4 Properties Span 83

Table 8: Properties of Span 83

Description[44]	Sorbitan Sesquioleata
Density[44]	989 kg/m3
Critical micelle concentration	180 ppm
Saturation IFT	20 $\mathrm{m\,N\,m^{-1}}$